Available online at www.sciencedirect.com
ScienceDirect
Geochimica et Cosmochimica Acta 73 (2009) 6868–6893
Geochimica et Cosmochimica Acta
www.elsevier.com/locate/gca

Iron partitioning and hydrogen generation during serpentinization of abyssal peridotites from 15°N on the Mid-Atlantic Ridge

Frieder Klein [a,*], Wolfgang Bach [a], Niels Jöns [a], Tom McCollom [b], Bruce Moskowitz [c], Thelma Berquó [c]

[a] Department of Geosciences, University of Bremen, Klagenfurter Str., 28359 Bremen, Germany
[b] CU Center for Astrobiology & Laboratory for Atmospheric and Space Physics, Campus Box 392, University of Colorado, Boulder, CO 80309, USA
[c] Institute for Rock Magnetism, Department of Geology and Geophysics, University of Minnesota, 310 Pillsbury Dr. SE, Minneapolis, MN 55455, USA

Received 13 April 2009; accepted in revised form 20 August 2009; available online 26 August 2009

Abstract

Aqueous dihydrogen (H_2,aq) is produced in copious amounts when seawater interacts with peridotite and H_2O oxidizes ferrous iron in olivine to ferric iron in secondary magnetite and serpentine. Poorly understood in this process is the partitioning of iron and its oxidation state in serpentine, although both impose an important control on dihydrogen production. We present results of detailed petrographic, mineral chemical, magnetic and Mößbauer analyses of partially to fully serpentinized peridotites from the Ocean Drilling Program (ODP) Leg 209, Mid-Atlantic Ridge (MAR) 15°N area. These results are used to constrain the fate of iron during serpentinization and are compared with phase equilibria considerations and peridotite–seawater reaction path models. In samples from Hole 1274A, mesh-rims reveal a distinct in-to-out zoning from brucite at the interface with primary olivine, followed by a zone of serpentine + brucite ± magnetite and finally serpentine + magnetite in the outermost mesh-rim. The compositions of coexisting serpentine (Mg# 95) and brucite (Mg# 80) vary little throughout the core. About 30–50% of the iron in serpentine/brucite mesh-rims is trivalent, irrespective of subbasement depth and protolith (harzburgite versus dunite). Model calculations suggest that both partitioning and oxidation state of iron are very sensitive to temperature and water-to-rock ratio during serpentinization. At temperatures above 330 °C the dissolution of olivine and coeval formation of serpentine, magnetite and dihydrogen depends on the availability of an external silica source. At these temperatures the extent of olivine serpentinization is insufficient to produce much hydrogen, hence conditions are not reducing enough to form awaruite. At $T < 330$ °C, hydrogen generation is facilitated by the formation of brucite, as dissolution of olivine to form serpentine, magnetite and brucite requires no addition of silica. The model calculations suggest that the iron distribution observed in serpentine and brucite is consistent with formation temperatures ranging from <150 to 250 °C and bulk water-to-rock ratios between 0.1 and 5. These conditions coincide with peak hydrogen fugacities during serpentinization and are conducive to awaruite formation during main stage serpentinization. The development of the common brucite rims around olivine is either due to an arrested reaction olivine → brucite → serpentine + brucite, or reflects metastable olivine–brucite equilibria developing in the strong gradient in silica activity between orthopyroxene (talc–serpentine) and olivine (serpentine–brucite).
© 2009 Elsevier Ltd. All rights reserved.

1. INTRODUCTION

Serpentinization of the oceanic lithospheric mantle is a widespread process, particularly along slow-spreading ridges, with significant consequences for rheology, chemis-

* Corresponding author. Tel.: +49 42121865405.
E-mail address: fklein@uni-bremen.de (F. Klein).

0016-7037/$ - see front matter © 2009 Elsevier Ltd. All rights reserved.
doi:10.1016/j.gca.2009.08.021

try and microbial habitability of the oceanic lithosphere (e.g., Dick, 1989; Cannat et al., 1992; Cannat, 1993; Escartín et al., 1997; Früh-Green et al., 2004; Iyer et al., 2008). A particular feature of serpentinization is the distinct chemical characteristics of related hydrothermal systems. Fluid pH_{25} ranging from 3 (at high temperatures) to 12 (at low temperatures), and exceedingly high hydrogen and methane concentrations make these systems one of the most extreme environments on Earth (Kelley et al., 2001; Charlou et al., 2002; Douville et al., 2002; Schmidt et al., 2007). The strongly reducing conditions found in continental and oceanic serpentinization settings are indicated by the presence of native metals/alloys (e.g., Nickel, 1959; Chamberlain et al., 1965; Eckstrand, 1975; Frost, 1985; Alt and Shanks, 1998; Beard et al., 2009; Klein and Bach, 2009). The enormous reduction potential is due to dihydrogen, which develops when H_2O oxidizes ferrous iron in primary minerals (e.g., olivine) to ferric iron in secondary phases, i.e., magnetite and serpentine minerals. Serpentinization does not only lead to the incorporation of iron in serpentine and magnetite. A large proportion of iron in serpentinites resides in brucite (Evans and Trommsdorff, 1972; Moody, 1976; D'Antonio and Kristensen, 2004; Bach et al., 2006; Seyfried et al., 2007). This is important for hydrogen production, because any ferrous Fe incorporated into brucite (and serpentine) leads to less hydrogen production.

Experimental and theoretical studies indicate that high H_2,aq concentrations during serpentinization are mirrored by low SiO_2,aq concentrations (Berndt et al., 1996; Wetzel and Shock, 2000; Allen and Seyfried, 2003; McCollom and Bach, 2009). Frost and Beard (2007) discussed the effect of silica activity (a_{SiO_2}) on magnetite formation and underscored that the presence and distribution of brucite is critical for the interpretation of serpentinization processes.

Although the Fe distribution between serpentine, magnetite and brucite is of importance for quantifying hydrogen production during serpentinization, only little attention has been paid to the mineral chemistry of brucite coexisting with serpentine and magnetite in abyssal serpentinites. Part of the problem is that comparisons of peridotite–seawater hydrothermal experiments and reaction path models with natural samples are rare. Also, brucite analyses from abyssal serpentinites are often not reported. From a data compilation of brucite–serpentine assemblages in alpine serpentinites, Evans and Trommsdorff (1972) retrieved a mean Fe–Mg distribution coefficient [$K_D = (X_{Fe}/X_{Mg})_{Srp} \cdot (X_{Mg}/X_{Fe})_{Brc}$] of 0.5. However, brucite compositions more ferroan than expected from this distribution coefficient are not uncommon (Hostetler et al., 1966; Page, 1967). Moody (1976) conducted an experimental study of serpentinization and reported $Fe(OH)_2$ contents in brucite as high as 18 mol.%, and pointed out an inverse correlation between Fe concentration in brucite and the amount of magnetite produced. Along those lines, Bach et al. (2006) suggested that magnetite forms from breakdown of Fe-rich brucite. However, these authors inferred brucite compositions from linear extrapolation of serpentine–brucite mixed analyses in abyssal serpentinites [Ocean Drilling Program (ODP) Leg 209]. Pure brucite with $Fe(OH)_2$ concentrations of up to 39 mol.% was reported by D'Antonio and Kristensen (2004) from serpentinite clasts recovered from the South Chamorro Seamount in the Mariana forearc (ODP Leg 195; e.g., Savov et al., 2007). It is clear that a more detailed and systematic analysis of coexisting serpentine–brucite pairs in abyssal serpentinites would help furthering our understanding of hydrogen production during serpentinization.

This communication reports detailed petrographic and mineral chemical data of partly to fully serpentinized peridotites from Ocean Drilling Program Leg 209 (MAR 15°N area). We link these observations with peridotite–seawater reaction path models and phase petrological considerations of the system $SiO_2-MgO-FeO-Fe_2O_3-H_2O$. The use of geochemical modeling facilitates the reconstruction of simultaneously changing heterogeneous phase equilibria of peridotite–seawater interaction. This study focuses on Fe distribution between serpentine, brucite and magnetite and its implications for hydrogen production during serpentinization. In addition, we evaluate dependencies of fluid–rock reaction paths on protolith compositions and compare our results with information provided by experimental and field investigations.

2. ANALYTICAL METHODS

2.1. Microscopy and electron microprobe analysis (EMPA)

Thin sections were optically investigated in transmitted and reflected light using a Leica DM RXP HC oil immersion microscope. Mineral compositions were analyzed with a 'JEOL Superprobe JXA 8900 R' electron microprobe at the University of Kiel (Germany), equipped with five wavelength-dispersive spectrometers. Minerals were analyzed with an accelerating voltage of 20 kV for a beam current of 15–20 nA and a fully focused 1 μm beam diameter. Both synthetic and natural mineral standards were used. Raw data were corrected using the CITZAF method of Armstrong (1995). Micro-scale element mappings and backscattered electron (BSE) images of serpentine meshes were used to complement petrographic observations.

2.2. Mößbauer spectroscopy and magnetization measurements

To quantify the amount of magnetite present and the distribution, coordination and oxidation state of iron in mesh-rims of partially to fully serpentinized peridotites, Mößbauer spectroscopic and magnetic investigations were carried out at the Institute for Rock Magnetism (IRM), University of Minnesota, USA. Mesh-rims of selected samples from Hole 1274A were micro-drilled and analyzed using Mößbauer spectroscopy with a conventional constant-acceleration spectrometer in transmission geometry. Hyperfine parameters such as magnetic hyperfine field (B_{HF}), isomer shift (IS) and quadrupole splitting (QS) have been determined by the NORMOS program (Brand, 1987), and α-Fe at room temperature was used to calibrate isomer shifts and velocity scale. Room temperature hysteresis loops were obtained in a vibrating sample magnetometer (Princeton Corporation Measurements) using

an electromagnet to produce fields up to 1 T. Low temperature remanent magnetization curves were performed with a SQUID magnetometer (Quantum Design, San Diego, CA, USA – MPMS-XL). The data were obtained by cooling the sample to 10 K in zero field and then giving a 2.5-T remanent magnetization. The resultant remanent magnetization was measured with increasing temperature up to 300 K.

2.3. Geochemical modeling

Calculations of equilibrium constants for dissolution of minerals, dissociation of aqueous species and redox reactions were made with the SUPCRT92 software code and database (Johnson et al., 1992). The SUPCRT92 database includes thermodynamic data from Helgeson et al. (1978) and Wolery and Jove-Colon (2004) for minerals, and Shock and Helgeson (1988), Shock et al. (1989, 1997) and Wolery and Jove-Colon (2004) for inorganic aqueous species. Further modifications include the addition of thermodynamic data for $NaSO_4^-$, $MgSO_4$ from McCollom (2000), aqueous Al complexes from Tagirov and Schott (2001), greenalite [$Fe_3Si_2O_5(OH)_4$], minnesotaite [$Fe_3Si_4O_{10}(OH)_2$] and ferroan brucite [$Fe(OH)_2$] from McCollom and Bach (2009). Volumetric data of ferroan brucite ($V^\circ = 26.43\ cm^3\ mol^{-1}$) were taken from Wolery and Jove-Colon (2004) since data from McCollom and Bach (2009) refer to amakinite ($30.5\ cm^3\ mol^{-1}$), which is not the pure Fe-endmember of the brucite solid solution. As experimentally derived thermodynamic data of Fe^{+3}-serpentine [$Fe_2Si_2O_5(OH)_4$] are not available we calculated the standard Gibbs free energy of formation (ΔG°_f) following the polyhedral sum approach of Chermak and Rimstidt (1989). Similarly, V° was calculated from polyhedral data given in Holland (1989). In these computations, hydroxide and oxide bonding of metals in the polyhedrons as well as metal coordination are accounted for. Standard heat capacity (C_p) and Maier–Kelley coefficients were calculated for Fe^{+3}-serpentine using Neumann–Kopp's rule and the reaction

$$\underset{Fe^{+3}\text{-serpentine}}{Fe_2Si_2O_5(OH)_4} + 3\underset{brucite}{Mg(OH)_2} = \underset{chrysotile}{Mg_3Si_2O_5(OH)_4} + 2\underset{bernalite}{Fe(OH)_3}. \quad (R1)$$

Heat capacity data of brucite and chrysotile were taken from Helgeson et al. (1978) and those of bernalite were taken from NIST (Chase, 1998). The standard molal third law entropy (S°) of Fe^{+3}-serpentine was estimated using the "analogue mineral algorithm" (Helgeson et al., 1978; Ransom and Helgeson, 1994) for reaction (R1). Thermodynamic data of Fe^{+3}-serpentine are summarized in Table 1.

Thermodynamic reaction path modeling was conducted using the computer code EQ3/6, version 8.0 (Wolery, 1992a,b) with a customized thermodynamic database assembled using SUPCRT92 (Johnson et al., 1992). The EQ3/6 database contains log K values for a constant pressure of 50 MPa and temperatures from 0 to 400 °C in 25 °C increments. For the calculation of activity coefficients of dissolved inorganic species we used the B-dot equation with hard core diameter, and B-dot and Debye–Hückel parameter from Wolery and Jove-Colon (2004). Activity coefficients are assumed to be unity for neutral species, except for non-polar gaseous species, for which the activity coefficients of CO_2 (Drummond, 1981) were assigned. Solid solutions we used in the reaction path models include serpentine (containing the endmembers chrysotile, greenalite, kaolinite, Fe^{+3}-serpentine), brucite (Mg-brucite, Fe-brucite), talc (talc, minnesotaite), orthopyroxene (enstatite, ferrosilite), clinopyroxene (diopside, hedenbergite), chlorite (clinochlore, daphnite) and tremolite (tremolite, Fe-actinolite). Serpentine in abyssal serpentinites is in most cases chrysotile or lizardite. Antigorite is common in alpine-type serpentinites but rarely found in abyssal serpentinites. As noted by Evans (2004) and Frost and Beard (2007) the differences between thermodynamic properties of chrysotile and lizardite are trivial and therefore we chose chrysotile to represent the Mg-endmember of serpentine (cf. Wilson et al., 2006). To account for Al in serpentine, we considered kaolinite [$Al_2Si_2O_5(OH)_4$] instead of amesite

Table 1
Calculated thermodynamic data of Fe^{+3}-serpentine.

Mineral	C_p°	a	$b \times 10^3$	$c \times 10^{-5}$	V°	S°
MgO*	9.03	10.18	1.74	−1.48	11.25	6.44
Fe_2O_3*	25.04	23.49	18.60	−3.55	30.27	20.94
$Mg_3Si_2O_5(OH)_4$*	52.90	75.82	31.60	−17.58	108.50	52.90
$Fe_2Si_2O_5(OH)_4$‡	50.85	68.77	44.98	−16.69	105.03	54.52
Polyhedral unit	g					
Fe_2O_3†	−185.49					
SiO_2†	−204.10					
H_2O†	−57.34					
$Fe_2Si_2O_5(OH)_4$§	$G^\circ_f = -708.36$					

C_p° = heat capacity (cal mol^{-1} K^{-1}); a, b, c = Maier–Kelley C_p-coefficients; V° (cm^3 mol^{-1}); S° (cal mol^{-1} K^{-1}); g (kcal mol^{-1}); G°_f (kcal mol^{-1}).

* Helgeson et al. (1978).

† Chermak and Rimstidt (1989).

‡ $Fe_2Si_2O_5(OH)_4 = Mg_3Si_2O_5(OH)_4 + Fe_2O_3 - 3MgO$.

§ $Fe_2Si_2O_5(OH)_4 = Fe_2O_3 + 2SiO_2 + 2H_2O$.

($Mg_2Al_2SiO_5(OH)_4$) in the solid solution model, because EQ6 is presently not capable of handling two ideal mixing sites of a solid solution. Besides olivine, the composition of which was fixed at Mg# 90 [(molar Mg/(Mg + Fe) × 100)] in the harzburgite models (cf. McCollom and Bach, 2009), all other solid solutions were allowed to vary freely over their entire compositional range. To account for metastable equilibria, we suppressed aragonite, calcite, dolomite, monticellite, magnesite, antigorite, hydroxyltopaz, huntite, wüstite, grossular and andradite. Moreover, the reduction of sulfate and carbon by dihydrogen was suppressed.

In total we calculated 12 isobaric ($p = 50$ MPa) reaction path models of two types. Type one models were calculated for temperatures from 25 to 400 °C at a water-to-rock ratio (w/r) of ~1. The second type of model was calculated for variable w/r ratios from virtually ∞ to ~0.2 at constant temperatures of 150, 200, 250, 300 and 350 °C.

2.3.1. Variable temperature (Type 1 models)

The advantage of computations with temperature as the only variable in a reaction path is the ease of examining the temperature dependence of heterogeneous phase equilibria for a rock composition of choice. The compositions selected in this study are (1) dunite (100% olivine, Mg# 90) and (2) harzburgite (Ol:Opx:Cpx = 80:15:5 in vol.%; see Table 2 for mineral compositions).

Each computation consists of several steps: at the beginning of each EQ3/6 calculation, EQ3NR is used to speciate 1 kg of solution (seawater, see Table 3 for composition) at 25 °C. Next, 1 kg of rock (dunite or harzburgite) is added and equilibrated with the solution in EQ6. The temperature is then incrementally increased to 400 °C, recalculating the equilibrium distribution of minerals and fluid species at each temperature. In effect, this determines the equilibrium compositions of minerals and fluid for the bulk system as a function of temperature. Since water is consumed during reaction with primary anhydrous minerals to form secondary hydrous minerals, the effective w/r deviates from unity in the equilibrium assemblage at low temperatures (w/r $\geqslant$ 0.7).

2.3.2. Variable w/r ratio (Type 2 models)

These models emulate the entrainment of heated seawater into fresh peridotite at a fixed temperature and pressure. We use dunite (olivine with Mg# 90) and harzburgite as the starting materials. Average w/r ratios in hydrothermal systems are believed to approximate unity (e.g., Mottl, 2002).

Table 2
Mineral compositions used as starting materials in reaction path models.

Atoms	Ol	Opx	Cpx
Si	1.00	1.98	1.99
Al		0.04	0.03
Fe	0.20	0.19	0.09
Mg	1.80	1.75	0.89
Ca		0.04	1.01
O	4.00	6.00	6.00
Mg#	90	90	91

Table 3
Initial fluid composition used in the models (mmol/kg).

Na^+	464.0
Cl^-	546.0
HCO_3^-	2.34
Ca^{2+}	10.2
Mg^{2+}	53.0
K^+	9.8
SiO_2,aq	0.11
Fe^{2+}	0.0000015
Al^{3+}	0.000037
SO_4^{2-}	28.2
O_2,aq	0.25
pH	7.8

Our models include a much larger range of w/r ratios to emulate phase equilibria from virtually incipient to complete serpentinization. We emphasize that at the incipient stage of serpentinization the w/r is infinitesimally low and that hydration will increase the ionic strength of the interacting fluids. The activity coefficients calculated by the B-dot equation are unreliable above ionic strengths > 1 molal (Wolery, 1992a). For this reason, all reaction paths were terminated at w/r ≈ 0.2.

The procedure for the variable w/r models is as follows: we speciate 1 kg of seawater at 25 °C using EQ3NR. We then simulate reaction of the seawater with a small amount of peridotite (1 g) during heating to the designated temperature (150, 200, 250, 300 and 350 °C). The reaction of seawater with a small amount of peridotite intends to emulate the high w/r conditions within a recharge zone before the seawater can hydrate the pristine mantle peridotite. To this fluid, we next add peridotite in small increments until a final w/r ratio of approximately 0.2 is reached. This procedure allows us to examine the equilibrium distribution and abundance of minerals and fluid species at water-to-rock ratios between 0.2 and 1000.

3. RESULTS

3.1. Petrography

Comprehensive geological descriptions of ODP Leg 209 Hole 1274A have been published elsewhere (Bach et al., 2004; Kelemen et al., 2004a,b; Paulick et al., 2006) and will not be repeated here.

Thin section investigation indicates that the serpentinites usually contain relics of primary olivine (~0–35 vol.%), orthopyroxene (~0–30 vol.%), clinopyroxene (~0–5 vol.%) and Cr-spinel (~0–2 vol.%). The primary modes were not determined explicitly but protoliths were dunite and harzburgite similar to those reported in Seyler et al. (2007). Peridotite from Hole 1274A shows an overall systematic downhole increase in the extent of serpentinization (Kelemen et al., 2004b). However, even on a thin-section scale, the extent of serpentinization is highly variable with fully replaced and unaltered primary minerals next to each other. The micro-textures of serpentinized peridotites range from pseudomorphic mesh and hourglass textures after olivine and bastite textures after pyroxene to transitional ribbon textures, to non-pseudomorphic and to interlocking tex-

tures. Most thin sections from Hole 1274A feature extensive paragranular and transgranular serpentine veining. Paragranular veins form an anastomosing network that wraps around porphyroclasts, whereas transgranular veins crosscut porphyroclasts (O'Hanley, 1996). Ni–Fe sulfides and alloys are present only in trace amounts. For a detailed description of Fe–Ni–Co–O–S phase relations in the same thin sections we refer to Klein and Bach (2009).

In the following section we focus on secondary hydrous silicates, oxides and hydroxides in pseudomorphic textures and veins. Due to the intimate intergrowth of serpentine and brucite, these minerals are in most cases indistinguishable with an optical microscope. To overcome this difficulty we used electron microprobe analyses (EMPA) for mineral identification.

3.1.1. Pseudomorphic mesh textures

In partially serpentinized rocks, mesh textures with olivine in the mesh center and α- or γ-serpentine and brucite in the mesh-rims are typical. Mesh-rims commonly reveal a distinct in-to-out zoning from reddish-brown brucite at the interface with olivine, followed by a zone of α-serpentine + brucite ± magnetite and finally α- or γ-serpentine and magnetite in the outermost mesh-rims (see Fig. 1). While the brucite abundance decreases, the proportions of magnetite and serpentine increase from center to rim of each individual mesh. Magnetite is dispersed throughout much of the mesh-rim and it becomes more abundant and coarser-grained near the rims. In many cases mesh-rims are bordered by trails of anhedral to subhedral magnetite with grain sizes ranging from less than 1 μm to more than

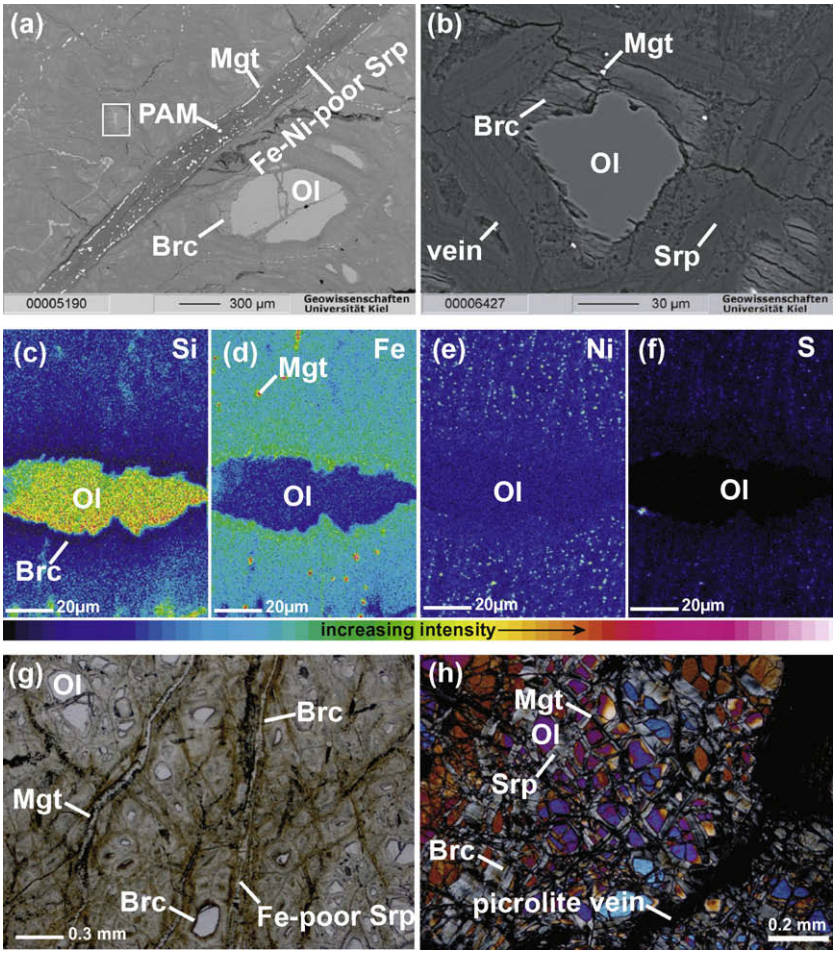

Fig. 1. Back-scattered electron images, element distribution maps and photomicrographs of partly serpentinized peridotites from Hole 1274A. (a) Transgranular serpentine vein crosscutting pseudomorphic mesh texture of dunite. Serpentine hosting abundant magnetite and Ni–Fe sulfides/alloys has low Fe and Ni contents. White box indicates the area mapped in (c–f) (sample 1274A-10R1, 3–10 cm). (b) Pseudomorphic serpentine (Mg# 95) and Fe-rich brucite (Mg# 80) growing after olivine. Magnetite is present in the brucite (Mg# 80) zone surrounding olivine and finely disseminated in serpentine surrounding brucite. Note the rugged interface of olivine and brucite indicating disequilibrium (sample 1274A-22R1, 24–32 cm) (c–f). Detail in (c) (white box). Element maps depicting Si, Fe, Ni and S in mesh-rim. Pure Fe-rich brucite (Mg# 80) is present at the interface with olivine. The proportion of serpentine relative to brucite increases from center to rim. The abundance of magnetite, Ni–Fe alloys, and sulfur-poor Ni–Fe sulfides increases from center to rim. (g) Mesh texture crosscut by para- and transgranular serpentine veins. Note brownish brucite along veins (plane polarized light; sample 1274A-10R1, 3–10 cm). (h) Picrolite vein crosscutting mesh texture. Magnetite forms a network tracing former olivine grain boundaries and intra-grain cracks (sample 1274A-6R2, 128–135 cm). (Ol, olivine; Srp, serpentine; Brc, brucite; Mgt, magnetite; PAM = pentlandite + awaruite + magnetite). (For interpretation of the references to color in this figure legend, the reader is referred to the web version of this article.)

50 μm. Weakly serpentinized olivine appears to retain its original crystal shape. A thin (ca. <10 μm) brucite zone surrounds olivine (as inferred by EMPA). With increasing extent of alteration, grain boundaries of olivine become progressively serrated, while the thickness of the brucite zone increases and develops a distinct reddish-brown color.

Nickeliferous opaque minerals are scarce at the interface between brucite and olivine, but their abundance and grain size increases from center to rim suggesting growth with progressive hydration of olivine (cf. Klein and Bach, 2009). Predominant nickeliferous opaque minerals are (Co-) pentlandite, awaruite and heazlewoodite.

3.1.2. Pyroxene alteration

Relics of orthopyroxene are commonly preserved. They contain exsolution lamellae of clinopyroxene parallel to the (1 0 0) plane. The pseudomorphic replacement of orthopyroxene, i.e., bastite, is by serpentine only; neither brucite nor magnetite is developed. Clinopyroxene is rare in rocks from Hole 1274A (cf. Seyler et al., 2007), but commonly preserved.

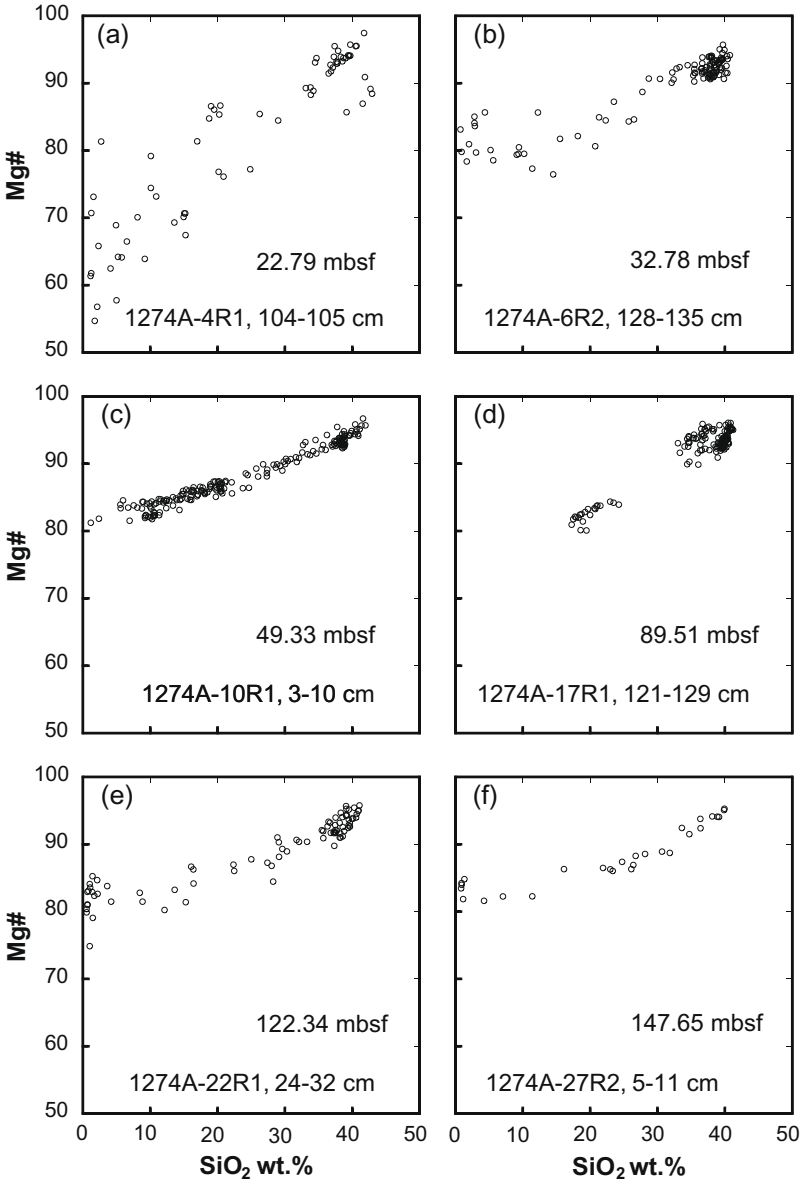

Fig. 2. Regression analyses of brucite and serpentine in mesh textures of rocks from Hole 1274A. (a) Sample 1274A-4R1, 104–105 cm contains both Fe-rich (Mg# 81) and extremely Fe-rich (Mg# ~55) brucite. (b) Sample 1274A-6R2, 128–135 cm contains brucite with a mean Mg# of 79 although some brucite has slightly elevated Mg# of ~85. (c) Sample 1274A-10R1, 3–10 cm exhibits a rather uniform brucite composition with Mg# 80. (d) In sample 1274A-17R1, 121–129 cm no pure brucite was detected, however, a rather low Mg# of 72 is indicated. Note the bimodal distribution. (e) Sample 1274A-22R1, 24–32 cm contains brucite with a mean Mg# of 81, however, the whole range is ~75–85. (f) Sample 1274A-27R2, 5–11 cm contains brucite a mean Mg# of 82 but Mg# is in places 85. Owing to the small grain size of secondary phases, virtually all microprobe analyses represent the composition of serpentine and brucite mixtures on a submicron scale. Brucite compositions are given at $SiO_2 = 0$ wt.%. Serpentine compositions are given at ~43 wt.% (depending on its Mg/Fe mass ratio).

3.1.3. Veins

Intra-grain veinlets in olivine consist of serpentine and finely dispersed magnetite. EMPA reveal slightly lower SiO_2 contents of the vein material near the olivine interface, which may point to the presence of brucite, but the existence of brucite could not unequivocally be verified. Para- and transgranular serpentine veins usually host abundant magnetite and nickeliferous opaque minerals. These occur in relatively coarse aggregates ($\leqslant$50 μm) and contrast with the finely dispersed opaque minerals ($\leqslant$2 μm) in intra-olivine veins or in mesh-rims. In para- and transgranular veins, magnetite is enriched along the margins, while γ-serpentine is concentrated in the vein center. Sigmoidal γ-serpentine veins are usually devoid of magnetite and nickeliferous phases. Para- and transgranular veins crosscutting mesh serpentine are generally bound by reddish-brown brucite, whereas sigmoidal veins lack brucite. The latest generation of transgranular serpentine veins (picrolite) are composite, laminated isotropic and anisotropic serpentine oriented parallel to both vein boundaries. They show trails of magnetite usually near the vein margins and are bordered by brown selvages with abundant brucite. Where picrolite veins crosscut bastite, they always lack magnetite and brucite.

3.2. Mineral compositions

Table A1 reports representative EMPA data for olivine, orthopyroxene, serpentine and brucite from ODP Hole 1274A (the complete set of analyses is available from the corresponding author upon request). Fig. 2 illustrates Mg–Fe distribution between serpentine and brucite in pseudomorphic mesh-rims. For comparison, Fig. 3 depicts EMPA data of both serpentine and brucite in mesh-rims, as well as serpentine and talc in bastite. In addition, EMPA profiles were used to investigate the mineral chemistry of serpentine, brucite and magnetite in spatial resolution (Fig. 4). Owing to the small grain size of secondary phases, virtually all microprobe analyses represent the composition of mineral mixtures on a submicron scale.

3.2.1. Primary silicates

Olivine has Mg#s between 90 and 93, CaO contents of 0.03–0.21 wt.%, 0.34–0.42 wt.% NiO, and CoO contents up to 0.05 wt.%. All olivine grains are chemically unzoned. Orthopyroxene has Mg# of 91–93 and CaO contents of 1.3–4.6 wt.%. It contains about 3 wt.% Al_2O_3 and 1.0 wt.% Cr_2O_3. Clinopyroxene is diopside-rich (Mg# 93–94) and contains about 3 wt.% Al_2O_3. The composition of clinopyroxene exsolution lamellae (<1 μm thickness) could not be determined. EMPA data of primary silicates reported by Moll et al. (2007) and Seyler et al. (2007) are in general agreement with our results.

3.2.2. Brucite

Regression analyses of brucite–serpentine mixtures in mesh-rims reveal fairly uniform Mg#s of brucite between 81 and 84 (see Figs. 2 and 3). More variable and Fe-rich compositions were determined for brucite from samples 1274A-4R1, 104–105 cm (Mg# >62; Fig. 2a) and 1274A-17R1, 121–129 cm (Mg# >72; Fig. 2d). Mg#s derived from

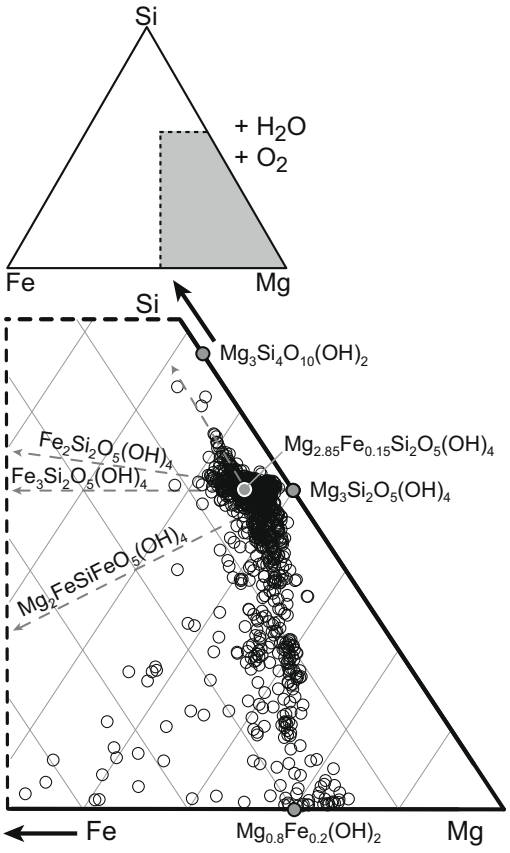

Fig. 3. Fe–Mg–Si ternary plot (molar proportions) projected from H_2O similar to that by Wicks and Plant (1979). Tie lines extend to hypothetical serpentine Fe^{+2} and Fe^{+3}-endmembers. Serpentine in mesh-rims contains both Fe^{+2} and Fe^{+3} as some analyses plot along lines to Fe^{+3}-serpentine, $Fe_2Si_2O_5(OH)_4$ and greenalite, $Fe_3Si_2O_5(OH)_4$. The presence of Mg-cronstedtite, $Mg_2FeSiFeO_5(OH)_4$, is not indicated. Most serpentine–brucite mixed analyses plot between serpentine (Mg# 95) and brucite (Mg# 80), however, samples 1274A-4R1, 104–105 cm and 1274A-17R1, 121–129 cm trend towards much higher Fe contents.

single point analyses of brucite (where SiO_2 <1 wt.%) are consistent with these results, although individual analyses scatter around the regression value. Individual analyses are, in some cases, strongly elevated in MnO (1.1 wt.%), CaO (0.6 wt.%) and Al_2O_3 (0.9 wt.%). Elevated sulfur concentrations (given as SO_3 in Table A1) are most likely related to Ni–Fe sulfides present in the brucite matrix. The actual concentrations of NiO and FeO in brucite (corrected for sulfide) are likely to be lower than shown in Table A1 by as much as 0.5 wt.%.

3.2.3. Serpentine

The composition of serpentine varies depending on its precursor mineral and textural context. Regression analyses reveal that serpentine in mesh-rims is more magnesian than olivine, with Mg#s ranging from 94 to 96 (Figs. 2 and 3). CaO contents are generally below 0.15 wt.%. The Al_2O_3 content is mostly below 0.1 wt.%, but may be up to 0.6 wt.%, possibly indicative of minor chlorite intergrown with serpentine. NiO is positively correlated with sulfur content, sug-

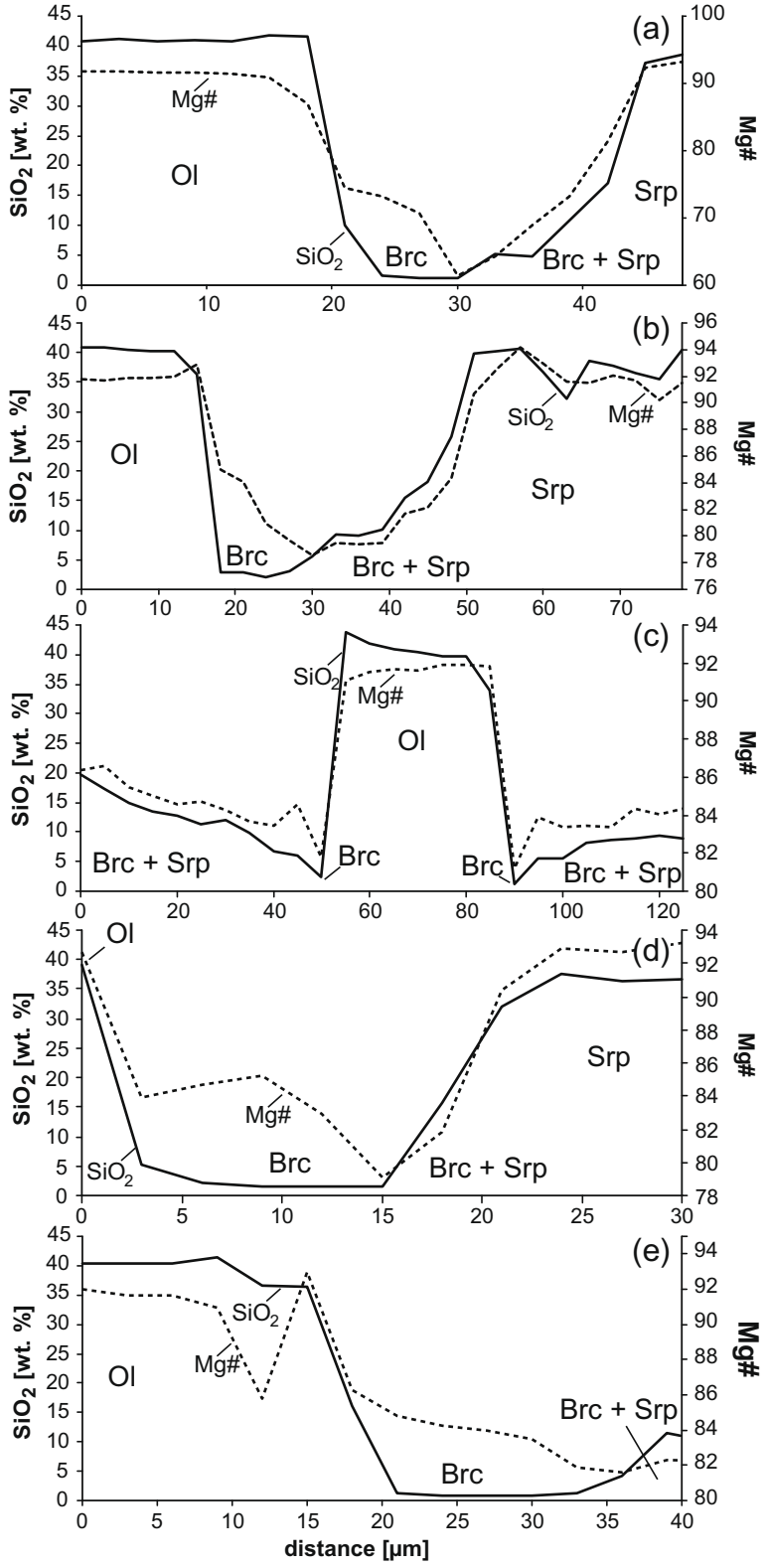

Fig. 4. Representative EMPA profiles through mesh-rims illustrating mineral zoning from relic olivine in the center, towards brucite and finally serpentine in the outermost mesh-rim. (a) 1274A-4R1, 104–105 cm, (b) 1274A-6R2, 128–135 cm, (c) 1274A-10R1, 3–10 cm, (d) 1274A-22R1, 24–32 cm, (e) 1274A-27R2, 5–11 cm.

gesting the presence of Ni–Fe sulfides in the serpentine matrix. Pseudomorphic serpentine after orthopyroxene (bastite) has Mg# ranging from 86 to 96 and high contents of CaO (<1.7 wt.%), Al_2O_3 (<2.6 wt.%), Cr_2O_3 (<1.2 wt.%),

MnO (<0.36 wt.%) and low contents of NiO (<0.2 wt.%) compared to mesh serpentine (Fig. 3 and Table A1). Serpentine associated with magnetite in para- and transgranular veins has Mg# between 94 and 98. In contrast, chrysotile in sigmoidal veins lacking magnetite, is more Fe-rich with Mg# ~92. CaO and Al_2O_3 contents of vein serpentine are similar to those of mesh serpentine. Serpentine in para- and transgranular veins hosting Ni–Fe sulfides and alloys has extremely low NiO contents <0.05 wt.%.

3.3. Mößbauer spectroscopy and bulk magnetization

Mesh-rims of partly to fully serpentinized peridotites were separated by micro-drilling to investigate $Fe^{+3}/\sum Fe$ values of serpentine and brucite and the relation between the oxidation state and the extent of serpentinization. Bulk magnetization analyses were conducted to relate $Fe^{+3}/\sum Fe$ values to magnetite contents of mesh-rims.

The spectra obtained (Fig. A1) where fitted by two sextets, corresponding to site A and B of magnetite, and three doublets, one associated with Fe^{+2} and two doublets of Fe^{+3} corresponding to tetrahedral and octahedral occupancy (Table 4). Samples 1274A-6R2, 128–135 cm and 1274A-22R1, 24–32 cm did not show sextet contributions; however, low temperature remanent magnetization curves for all samples including 1274A-6R2, 128–135 cm and 1274A-22R1, 24–32 cm show the characteristic phase transition at 120 K associated with the Verwey Transition in magnetite. Bulk magnetization analyses and thin-section petrography revealed a positive correlation of magnetite content with extent of serpentinization. Where relict olivine is present, the magnetite content is significantly lower compared to fully serpentinized rocks. In weakly serpentinized peridotites, where magnetite is generally sparse, Mößbauer spectra revealed $Fe^{+3}/\sum Fe$ values between 0.30 and 0.48 of hydrous secondary phases (Table 4). In strongly to fully serpentinized peridotites hosting abundant magnetite, $Fe^{+3}/\sum Fe$ values are consistently higher and range from 0.53 to 0.68. Trivalent Fe is present in both tetrahedral and octahedral sites of serpentine. It appears that trivalent Fe occupies preferentially the octahedral site, since its relative area is larger than the area of tetrahedral site (see Fig. A1). In one sample (1274A-22R1, 24–32 cm) we analyzed the bulk magnetization and $Fe^{+3}/\sum Fe$ of separated bastite. Magnetization analysis confirms that bastite hosts almost no magnetite. The Mößbauer spectra indicate that about one third of the total Fe is trivalent. Where present, results of wet chemical titration analyses (Paulick et al., 2006) of bulk rock powders are in a good agreement with Mößbauer results for the mesh-rims.

3.4. Geochemical reaction path modeling

Thermodynamic calculations have been used for several decades to examine the conditions of metamorphic hydration of peridotites (e.g., Olsen, 1963; Evans et al., 1976; Berman et al., 1986; Früh-Green et al., 2004). In these studies, intensive parameters of serpentinization (for example, pressure and temperature) were estimated from univariant phase equilibria in the system $MgO-SiO_2-H_2O$. Univariant phase equilibria are suitable to examine alteration conditions for rocks of known composition, but this approach has little predictive value for speciation of interacting fluids. Furthermore, the influence of solid solutions on phase equilibria in serpentinites has been largely disregarded in this approach, even though solid solutions in serpentinites exhibit a wide compositional range. In particular, the significance of Fe–Mg exchange equilibria between serpentine and brucite has been emphasized recently by Evans (2008). Sleep et al. (2004) examined the effect of Fe partitioning into serpentine and brucite on hydrogen production during serpentinization, assuming a fixed Fe–Mg distribution coefficient of 0.5. Their approach constitutes a useful extension of pure endmember phase equilibria, but still imposes too many constraints to allow a full assessment of fluid–rock equilibria. Geochemical reaction path modeling codes such as EQ3/6 (Wolery, 1992a,b; Wolery and Daveler, 1992; Wolery and Jarek, 2003) can be used to gain deeper insights into the evolution of fluid and rock compositions during serpentinization. Several studies have used reaction path modeling to investigate various aspects of fluid–rock interaction during serpentinization (Wetzel and Shock, 2000; Palandri and Reed, 2004; Foustoukos et al., 2008; McCollom and Bach, 2009; Jöns et al., 2009). However, one of the main limitations of previous geochemical reaction path modeling studies is that the uptake of

Table 4
Mößbauer spectroscopy and bulk magnetization results of micro-drilled mesh-rims.

Sample	Mößbauer					Titration[a]	Magnetization
	% Fe_3O_4	Fe^{+2}	Fe^{+3} (IV)	Fe^{+3} (VI)	$Fe^{+3}/\sum Fe$	$Fe^{+3}/\sum Fe$	% Fe_3O_4
1274A-6R2, 128–135 cm	0	47	18	35	0.48	0.45	0.33
1274A-10R1, 3–10 cm	14	28	27	32	0.68	0.62	0.79
1274A-15R1, 106–114 cm	23	26	9	42	0.66	0.68	1.38
1274A-17R1, 121–129 cm	21	37	6	36	0.50	0.56	1.20
1274A-20R1, 121–126 cm	53	17	12	18	0.66	0.68	2.80
1274A-22R1, 24–32 cm	0	69	16	15	0.30	0.57	0.16
1274A-27R2, 5–11 cm	11	43	23	23	0.53	0.51	0.79
1274A-22R1, 24–32 cm[b]	0	65	24	11	0.34	0.57	0.43

(IV), tetrahedral coordination; (VI), octahedral coordination.
[a] Data from Paulick et al. (2006).
[b] Mößbauer spectroscopic and magnetization results of micro-drilled bastite.

Fe^{+3} into serpentine has not been considered, although it is well documented that serpentine can contain significant amounts of Fe^{+3} (Page, 1968; Whittaker and Wicks, 1970; Blaauw et al., 1979; Rozenson et al., 1979; O'Hanley and Dyar, 1993; González-Mancera et al., 2003; Seyfried et al., 2007). The reaction path models presented in this communication expand beyond those of previous studies as they additionally explore the uptake of Fe^{+3} in serpentine, which has a significant impact on hydrogen generation during peridotite–seawater interactions. Note that there is a conspicuous lack of knowledge concerning the Fe^{+3} uptake by brucite during serpentinization. Although it appears possible that brucite contains Fe^{+3}, we do not account for this in the solid solution model of brucite.

3.4.1. Serpentinization of olivine (Mg# 90) between 400 and 25 °C at w/r ≈ 1 (Model 1A)

This reaction path model investigates the isobaric retrograde hydration of monomineralic dunite in a closed system. Fig. 5 depicts a summary of the model results for equilibrium mineral assemblages and compositions of minerals and fluids as a function of temperature. At 400 °C olivine dominates the equilibrium mineral assemblage, accompanied by trace amounts of serpentine and magnetite (Fig. 5a). With decreasing temperature the amounts of serpentine and magnetite increase at the expense of olivine according to the generalized reaction:

$$\text{olivine} + SiO_2,\text{aq} + H_2O \rightarrow \text{serpentine} + \text{magnetite} + H_2,\text{aq}. \quad \text{(R2)}$$

As the formation of serpentine according to (R2) consumes dissolved silica, the SiO_2,aq activity drops (Figs. 5a and f, and 10, see white dashed line). It is important to note that the dearth of aqueous silica hampers the serpentinization of olivine in a dunite and thus the effective formation of magnetite and H_2,aq (Fig. 5a, c and f; (R2)). Reaction (R2) proceeds to the right with decreasing temperature, lowering $a_{SiO_2,aq}$ further until the system reaches a quasi-invariant point of olivine (Mg# 90) + serpentine (Mg# 99) + brucite (Mg# 96) + magnetite at 330 °C (Figs. 5a and b). Here, olivine breaks down completely and brucite becomes part of the stable equilibrium mineral assemblage according to the generalized reaction:

$$\text{olivine} + H_2O \rightarrow \text{serpentine} + \text{brucite} + \text{magnetite} + H_2,\text{aq}. \quad \text{(R3)}$$

Note that the emergence of brucite facilitates instantaneously the breakdown of olivine and the coincident formation of large amounts of magnetite and serpentine (Fig. 5a). In association with this complete reaction of olivine, H_2,aq increases steeply and peaks at around 387 mmolal (mM, see Fig. 5c). Concomitantly, the activity of H_2O decreases as H_2O is incorporated into serpentine and brucite (Fig. 5e). As (R3) is not dependent on silica, the lack of an external source of silica is no longer stabilizing olivine and the reaction is solely driven by the decrease in temperature. After olivine has completely reacted out (i.e., at $T < 320$ °C), H_2,aq and SiO_2,aq are controlled by equilibria between serpentine, brucite and magnetite, the typical phase assemblage found in completely serpentinized dunites. The amount of serpentine remains essentially constant with decreasing temperature (because the amount is constrained by the amount of SiO_2 in the bulk system), whereas the proportion of brucite increases steadily. Furthermore, serpentine and in particular brucite become increasingly Fe-rich as the temperature decreases (Fig. 5b and h). This is due to the temperature-dependent changes in sub-reactions of the brucite–serpentine–magnetite equilibrium that increase the stability of the Fe-endmembers of serpentine and brucite relative to magnetite. That is, the equilibrium constants for (R4)–(R6) increasingly favor the products with decreasing temperature:

$$\underset{\text{magnetite}}{Fe_3O_4} + H_2O + H_2,\text{aq} + 2SiO_2,\text{aq} = \underset{\text{greenalite}}{Fe_3Si_2O_5(OH)_4}. \quad \text{(R4)}$$

$$\underset{\text{magnetite}}{Fe_3O_4} + 2H_2O + H_2,\text{aq} = 3\underset{\text{Fe-brucite}}{Fe(OH)_2}. \quad \text{(R5)}$$

$$2\underset{\text{magnetite}}{Fe_3O_4} + 7H_2O + 6SiO_2,\text{aq} = 3\underset{\text{Fe}^{+3}\text{-serpentine}}{Fe_2Si_2O_5(OH)_4} + H_2,\text{aq}. \quad \text{(R6)}$$

Shifting the equilibria of (R4) and (R5) to the right reduces the amount of H_2 present at equilibrium. Overall H_2,aq drops with decreasing temperature, which is mainly driven by (R5). The activity of SiO_2,aq is controlled by fluid–rock equilibria (and buffered by specific mineral assemblages, e.g., serpentine–brucite) so that drive to make (or consume) hydrogen is implicitly accounted for in the reaction path model. As (R4)–(R6) proceed to the right side with decreasing temperature, magnetite is completely exhausted below 165 °C and the system is entirely controlled by exchange equilibria among serpentine and brucite (Fig. 5a). The H_2,aq activity is now dependent on the stability of Fe^{+3}-serpentine (Fig. 5b–d):

$$2\underset{\text{greenalite}}{Fe_3Si_2O_5(OH)_4} + 2SiO_2,\text{aq} + 5H_2O = 3\underset{\text{Fe}^{+3}\text{-serpentine}}{Fe_2Si_2O_5(OH)_4} + 3H_2,\text{aq}. \quad \text{(R7)}$$

$$2\underset{\text{Fe-brucite}}{Fe(OH)_2} + 2SiO_2,\text{aq} + H_2O = \underset{\text{Fe}^{+3}\text{-serpentine}}{Fe_2Si_2O_5(OH)_4} + H_2,\text{aq}. \quad \text{(R8)}$$

According to (R6)–(R8) at low temperatures the stability of Fe^{+3}-serpentine, and thus the activity of H_2,aq, is limited by the low SiO_2,aq activity, which is chiefly buffered by reaction:

$$\underset{\text{serpentine}}{Mg_3Si_2O_5(OH)_4} + H_2O = 2SiO_2,\text{aq} + 3\underset{\text{brucite}}{Mg(OH)_2}. \quad \text{(R9)}$$

With the exhaustion of magnetite, serpentine becomes increasingly magnesian as temperatures drop, while brucite becomes increasingly rich in iron (Fig. 5b; (R8) and (R9)).

The pH of the fluid, illustrated in Fig. 5e, increases from 4.8 at 400 °C to 9 at 25 °C. As proposed by McCollom and Bach (2009) the pH is largely determined by the stability of brucite, but is ultimately controlled by the entire mineral assemblage. Except for high temperatures, dissolved Ca and Mg are slightly enriched compared to the original fluid

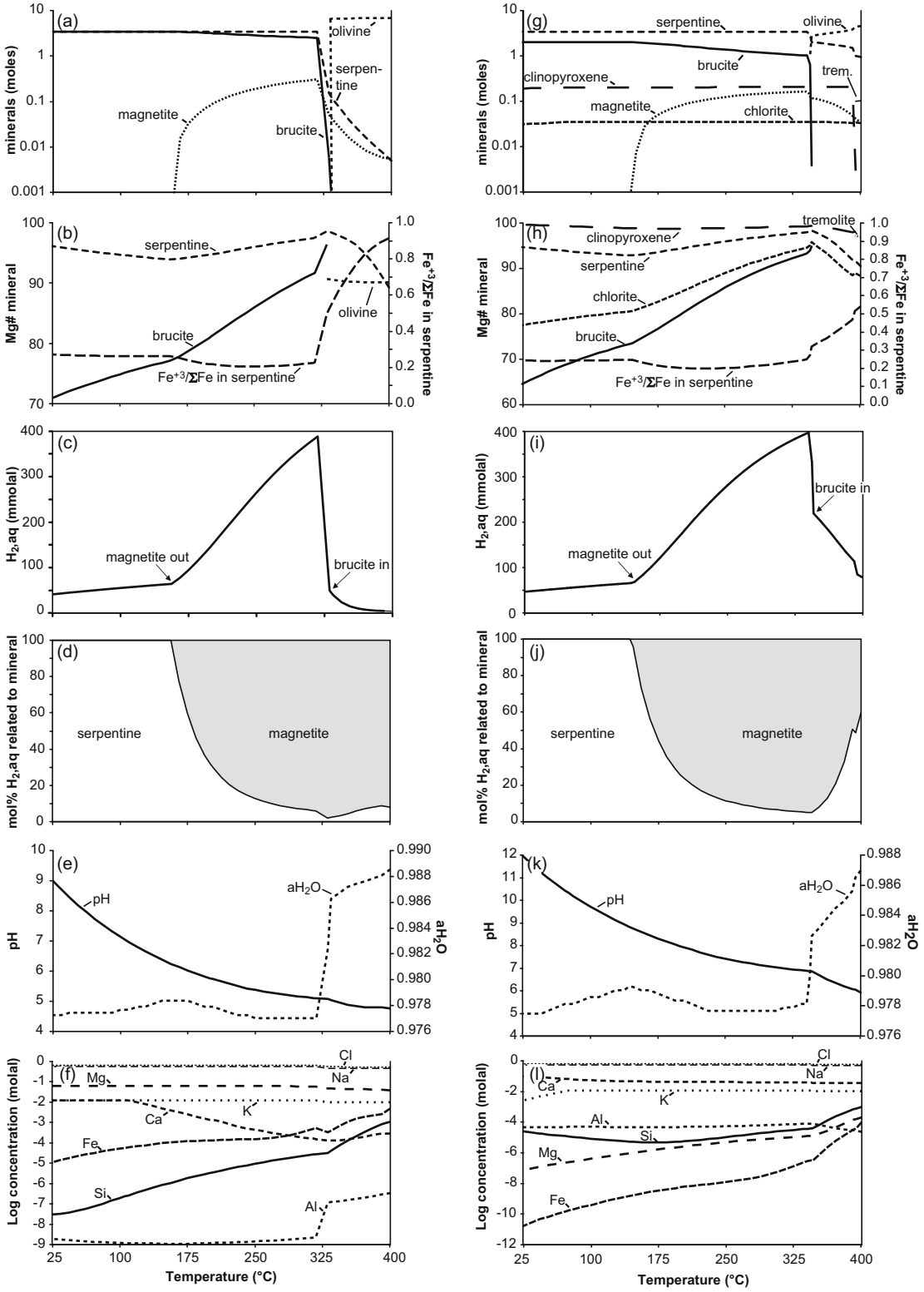

Fig. 5. Predicted alteration mineralogy and fluid composition of reaction path Models 1A and 1B, in which 1 kg of seawater equilibrated with 1 kg of dunite (a–f) and harzburgite (g–l), respectively, at temperatures between 25 and 400 °C. See text for discussion.

(Fig. 5f). The concentration of Fe exhibits a strong temperature dependency with increasing concentrations towards higher temperatures, reflecting buffering by changing phase assemblages described earlier.

3.4.2. Serpentinization of harzburgite between 400 and 25 °C at w/r ≈ 1 (Model 1B)

The rock composition used as the starting material in our calculations represents a harzburgite (Ol:Opx:Cpx = 80:15:5 vol.%). Although Cr-spinel is widespread in oceanic serpentinites, we ignored it in our calculations, because it remains largely unaltered in most samples from Hole 1274A (cf. Klein and Bach, 2009).

Fig. 5g–l summarizes the model results in terms of equilibrium mineral assemblages and compositions of minerals and fluids as a function of temperature. At 400 °C the equilibrium mineral assemblage consists of olivine, serpentine and tremolite as well as minor amounts of magnetite (Fig. 5g). The predicted concentration of H_2,aq is higher compared to Model 1A, because orthopyroxene provides the SiO_2 needed to produce serpentine and magnetite (Fig. 5i) according to the generalized reaction:

$$\text{olivine} + \text{orthopyroxene} + H_2O \rightarrow \text{serpentine} + \text{magnetite} + H_2, \text{aq}. \quad \text{(R10)}$$

At temperatures above the quasi-invariant point of olivine–serpentine–brucite equilibrium, concentrations of SiO_2,aq are slightly lower than predicted in Model 1A (Fig. 5l), because more serpentine is produced according to (R10). Diopsidic clinopyroxene is predicted to form at the expense of tremolite, which is unstable at temperatures below 390 °C

$$\underset{\text{tremolite}}{Ca_2Mg_5Si_8O_{22}(OH)_2} + H_2O = 2SiO_2, \text{aq} + 2\underset{\text{diopside}}{CaMgSi_2O_6} + \underset{\text{serpentine}}{Mg_3Si_2O_5(OH)_4}. \quad \text{(R11)}$$

The lower silica activity in Model 1B causes brucite to form at slightly higher temperatures (346 versus 330 °C). The emergence of brucite facilitates the formation of magnetite and serpentine at the expense of olivine according to (R3), resulting in H_2,aq concentrations of 397 mM at 340 °C. The predicted maximum concentration of H_2,aq is similar to that in the reaction path model with pure olivine, but H_2,aq is predicted to peak at a considerably higher temperature due to the shift of the quasi-invariant point of olivine–serpentine–brucite. As the temperature decreases, the concentration of H_2,aq drops when magnetite breaks down and Fe is taken up by brucite, serpentine and chlorite solid solutions. The amounts of serpentine, clinopyroxene and chlorite remain virtually constant with decreasing temperature, whereas the amount of brucite increases. Serpentine, chlorite and brucite become enriched in Fe as temperatures decrease, consuming magnetite (see (R4)–(R6)) until it is exhausted at $T < 146$ °C. At yet lower temperatures concentrations of H_2,aq and SiO_2,aq are buffered to low values by serpentine–brucite equilibrium (Fig. 5l). Owing to a speciation change from SiO_2,aq to $HSiO_3^-$ at pH ~8.5 the concentration of SiO_2,aq rises somewhat at $T < 165$ °C (Fig. 5k). The higher pH compared to Model 1A is related to the breakdown of primary clinopyroxene and orthopyroxene (with a Ca-Tschermak's component). These reactions also liberate significant amounts of Ca to the fluid. At temperatures below 346 °C, brucite–clinopyroxene–serpentine equilibrium sets the pH, which increases steadily as temperatures drop (Foustoukos et al., 2008). Concentrations of dissolved magnesium are low over the entire temperature range and are buffered by serpentine, brucite and clinopyroxene. Serpentine is more Fe-rich than serpentine in Model 1A and more serpentine is produced due to the higher amount of SiO_2 in the system (Fig. 5g and h). Consequently, predicted concentrations of dissolved Fe are markedly lower than in Model 1A. However, the strongly alkaline fluids (buffered by serpentine, brucite and clinopyroxene) are predicted to keep the concentrations of dissolved Fe low.

3.4.3. Serpentinization as a function of water-to-rock ratio (Model 2)

We next treat serpentinization as an isothermal process and compute the effect of changing water-to-rock ratios (w/r) on fluid–rock equilibria. Titration calculations, in which equal amounts of rock are added to 1 kg of seawater, are used to evaluate changes in mineralogy and fluid composition at five temperatures (150, 200, 250, 300 and 350 °C). Again we use olivine (Mg# 90) and harzburgite (Ol:Opx:Cpx = 80:15:5 vol.%) as the starting materials. Predicted fluid compositions, mineral assemblages and solid solution compositions of serpentine and brucite are illustrated in Fig. 6 as a function of w/r. In general, an increasing fraction of the initial amount of water is incorporated into hydrous phases with decreasing w/r. Consequently, the concentrations of non-reactive dissolved elements increase steadily with decreasing w/r.

3.4.4. Serpentinization of olivine (Mg# 90) at constant temperature (Model 2A)

At 150 °C the predicted equilibrium assemblage consists mainly of equal molar amounts of serpentine and brucite (Fig. 6a). Trace amounts of magnetite are predicted to occur only between w/r ≈ 1 and 40. Brucite composition is highly sensitive to changing w/r, as its Mg# decreases from 91 at high w/r to 76 at low w/r (Fig. 6k). The Mg# of serpentine decreases from 97 at high to 94 at low w/r. At high w/r virtually all Fe in serpentine is predicted to be trivalent, whereas at low w/r only 20 mol.% of the total Fe is ferric (Fig. 6k). The lowering in $Fe^{+3}/\sum Fe$ of serpentine is related to decreasing SiO_2,aq and H_2O activities as well as increasing H_2,aq activities at lower w/r (Figs. 6p and 7; cf. (R7)). With the predicted disappearance of magnetite at w/r ~ 1, H_2,aq concentration are no longer buffered by equilibria (R4)–(R6), causing a change in slope in H_2 versus w/r (Fig. 7). Equilibria (R7) and (R8) should now govern H_2 activities, and although Fe^{+3}-serpentine decreases in abundance (Fig. 6k), H_2 increases, because the system becomes more rock dominated. The pH is largely controlled by the solubility of serpentine and brucite, and Mg^{2+} is the dominant cation apart from Na^+ over the entire w/r range. Concentrations of dissolved elements (Fig. 6p), except for Al (not shown), remain constant or increase slightly with decreasing w/r (see above). Aluminum in the fluid decreases due to incorporation in serpentine (kaolinite component).

At 200, 250 and 300 °C serpentine and brucite dominate the equilibrium mineral assemblage over the entire w/r range (Fig. 6b–d), similar to the model at 150 °C. The main difference is that magnetite does not break down at w/r < 1. As we have already shown in the temperature-dependent

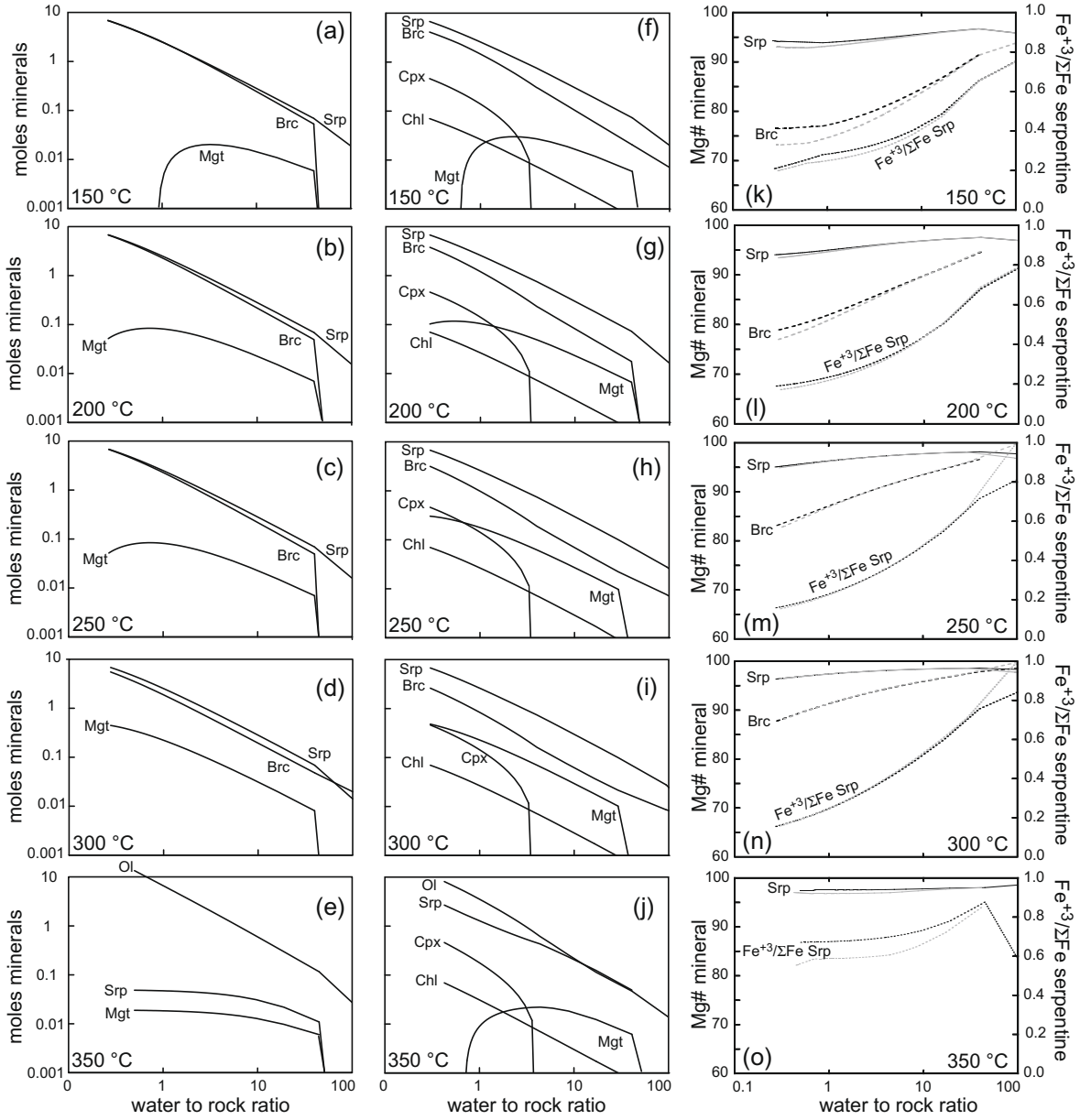

Fig. 6. Predicted alteration mineralogy and fluid composition of reaction path Models 2A and 2B at constant temperature as a function of water-to-rock ratio. (a–e) predicted equilibrium mineral assemblage for Model 2A; (f–j) equilibrium mineral assemblage predicted for Model 2B; (k–o) predicted mineral composition of serpentine and brucite; black lines denote mineral compositions for Model 2A, grey lines denote mineral compositions for Model 2B. (p–t) predicted fluid composition for Model 2A; (u–y) predicted fluid composition for Model 2B. See text for discussion.

model, serpentine and brucite become increasingly magnesian at higher temperatures, promoting magnetite formation. The amount of magnetite is expected to increase steadily with decreasing w/r, albeit not as much as the abundance of serpentine and brucite. In accordance with the corresponding temperature-dependent Model 1A (Fig. 5), predicted concentrations of H_2,aq increase considerably from 150 to 300 °C (see Fig. 7). Moreover, at low w/r, concentrations of dissolved H_2 are predicted to increase almost exponentially with decreasing w/r. Concentration changes of the dissolved elements are very similar to those of the 150 °C model, although absolute concentrations differ (Fig. 6p–t). In particular, concentrations of dissolved Si, Fe and Al are slightly higher whereas those of all other dissolved elements are lower (as it is expected from the equivalent temperature-dependent Model 1A) at the corresponding w/r.

At 350 °C the equilibrium phase assemblage is predicted to consist mainly of olivine with minor amounts of serpentine and magnetite (Fig. 6e), reflecting the enhanced stability of olivine at $T > 330$ °C. Consequently, $a_{H_2,aq}$ is low and concentrations of dissolved elements are elevated compared to concentrations of dissolved elements at lower temperatures.

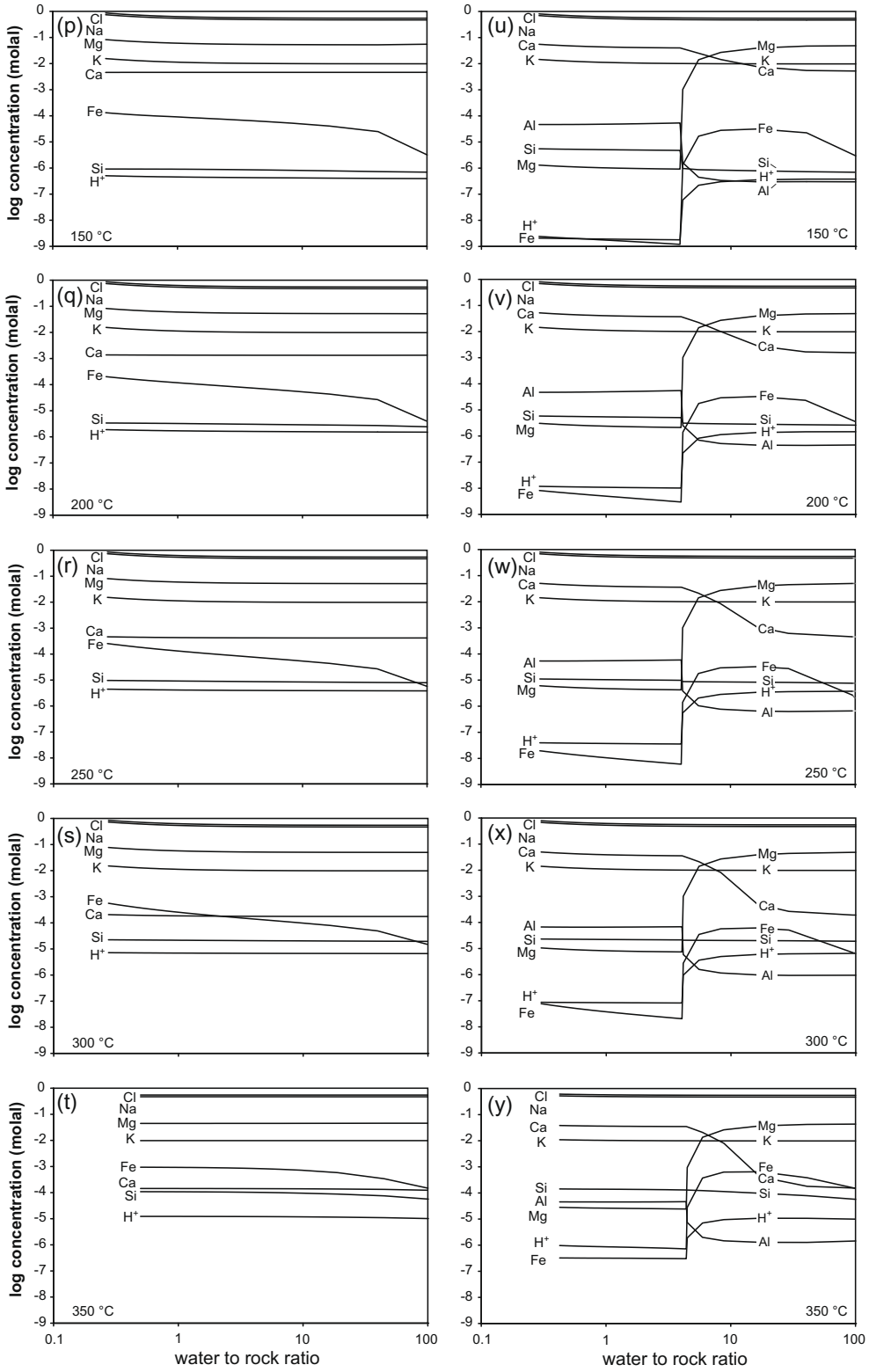

Fig. 6 (*continued*)

3.4.5. Serpentinization of harzburgite at constant temperature (Model 2B)

At 150 °C and w/r > 4 the equilibrium assemblage produced by the hydration of harzburgite is predicted to consist mainly of serpentine and brucite with minor magnetite (at w/r < 40, Fig. 6f) and trace amounts of chlorite. At a w/r ⩽ 4 secondary clinopyroxene becomes part of the equilibrium assemblage. Magnetite is predicted to

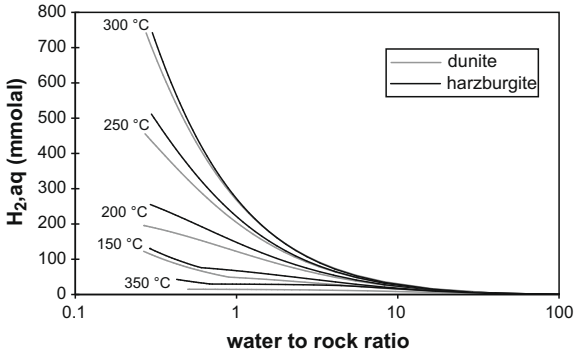

Fig. 7. Predicted dihydrogen generation for serpentinization of dunite (grey lines) and harzburgite (black lines) at constant temperature as a function of water-to-rock ratio. See text for discussion.

disappear at w/r < 0.6, i.e., at a somewhat lower w/r than in Model 2A. The evolution of the solid solution compositions of serpentine and brucite is almost identical with that of Model 2A (Fig. 6k). Clinopyroxene is essentially pure diopside. Chlorite appears in the assemblage as the primary host of Al, but makes up only a small fraction of the solid products. Its composition evolves from pure clinochlore at high w/r to more ferroan chlorite (20 mol.% daphnite) at low w/r. Hydrogen concentrations are consistently higher compared to Model 2A, but again, H_2,aq concentrations increase slightly at low w/r, when magnetite disappears, reflecting H_2,aq buffering by Fe^{+3}-serpentine (kink in trend in Fig. 7).

At high w/r ratios the pH is buffered by serpentine and brucite to values around 6.5, whereas at w/r $\leqslant$ 4 pH is buffered by secondary clinopyroxene, serpentine and brucite to higher values around 8.6 (cf. Foustoukos et al., 2008). This is reflected by concentrations of dissolved Mg and Ca. The concentration of Mg is high (~52 mmol/kg) at high w/r ratios and decreases slightly along with progressive formation of serpentine and brucite. At w/r $\leqslant$ 4, where clinopyroxene is predicted to be part of the equilibrium assemblage, the concentration of Mg decreases drastically to low values ~1 μmol/kg. Calcium, liberated by dissolution of primary clinopyroxene and the CaTs-component of orthopyroxene, is only partly incorporated into secondary clinopyroxene, resulting in increasing concentrations of Ca with decreasing w/r ratio.

At 200, 250 and 300 °C the equilibrium mineral assemblage is essentially the same as in the model at 150 °C, however, the main difference is the strong increase of the amount of magnetite towards lower w/r and thus consistently higher H_2,aq concentrations at higher temperatures. In addition, concentration patterns of dissolved elements relative to w/r are very similar to those of the model at 150 °C although shifted to higher concentrations for most elements.

In contrast to Model 1A, at 350 °C the equilibrium phase assemblage is predicted to consist mainly of serpentine and olivine with minor amounts of clinopyroxene, chlorite and magnetite (Fig. 6e).

In general, the presence of orthopyroxene in harzburgite means the bulk rock composition has a higher proportion of Si than in dunite, allowing a greater fraction of serpentine in the equilibrium assemblage. In this respect, during serpentinization of harzburgite two factors permit higher concentrations of H_2,aq compared with serpentinization of dunite: (1) Since serpentine accommodates less Fe in its structure than brucite, a higher proportion of Si results in greater amounts of magnetite and (2) promotes a higher proportion of Fe^{+3}-serpentine relative to greenalite.

3.4.6. *Fe–Ni–O–S phase relations*

The most abundant Fe–Ni–O–S assemblage in partly serpentinized rocks is pentlandite [$(Fe,Ni,Co)_9S_8$] + awaruite (Ni_3Fe) + magnetite, followed by pentlandite + heazlewoodite (Ni_3S_2) + magnetite in partly to completely serpentinized rocks (Klein and Bach, 2009). At increasingly reducing conditions, pentlandite is desulfurized to awaruite and/or heazlewoodite – the sulfide-phase representing the lowest S fugacity.

In agreement with the petrologic observations of Klein and Bach (2009), our reaction path models predict the desulfurization of pentlandite to low sulfur fugacity Ni-phases awaruite and/or heazlewoodite (Fig. 8). Consistent with calculations by Frost (1985), Fe–Ni–O–S phase equilibria reveal a strong dependency on the total sulfur ($\sum$S) content of the system. At low $\sum$S concentrations pentlandite will be desulfurized and the system proceeds towards heazlewoodite + awaruite + magnetite, whereas at somewhat higher $\sum$S concentrations pentlandite will form an assemblage together with heazlewoodite and magnetite.

Minimum H_2,aq concentrations required to stabilize the pentlandite + awaruite + magnetite assemblage increase from ~150 mM at 150 °C to almost 4 M at 400 °C (Klein and Bach, 2009). The modeling results reveal that serpentinization of dunite and harzburgite yields insufficient H_2,aq above ~330 °C to stabilize this assemblage (cf. Figs. 5 and 7). Below a temperature of ~330 °C, it depends on the w/r whether this assemblage is stable or not, since serpentinization produces more H_2,aq at lower w/r ratios (Fig. 7).

4. DISCUSSION

4.1. Serpentinization at Hole 1274A and geochemical reaction path models

Our modeling results allow an assessment of the temperature and w/r dependencies of Fe–Mg equilibria between serpentine, brucite and magnetite. The models predict that serpentine incorporates increasing amounts of iron with decreasing temperature and w/r (Figs. 5 and 6) as long as magnetite and brucite are present. Brucite behaves similarly and becomes increasingly Fe-rich with decreasing w/r and temperature. However, the Fe-enrichment of brucite at lower temperatures is much more pronounced than that of serpentine. The temperature dependency of Fe–Mg equilibria is mirrored by the temperature dependency of redox conditions during serpentinization, and concomitantly monitored by Fe–Ni–Co–O–S phases. Hence, before modeled Fe–Mg equilibria for coexisting serpentine, brucite and magnetite can be adopted for samples from Hole

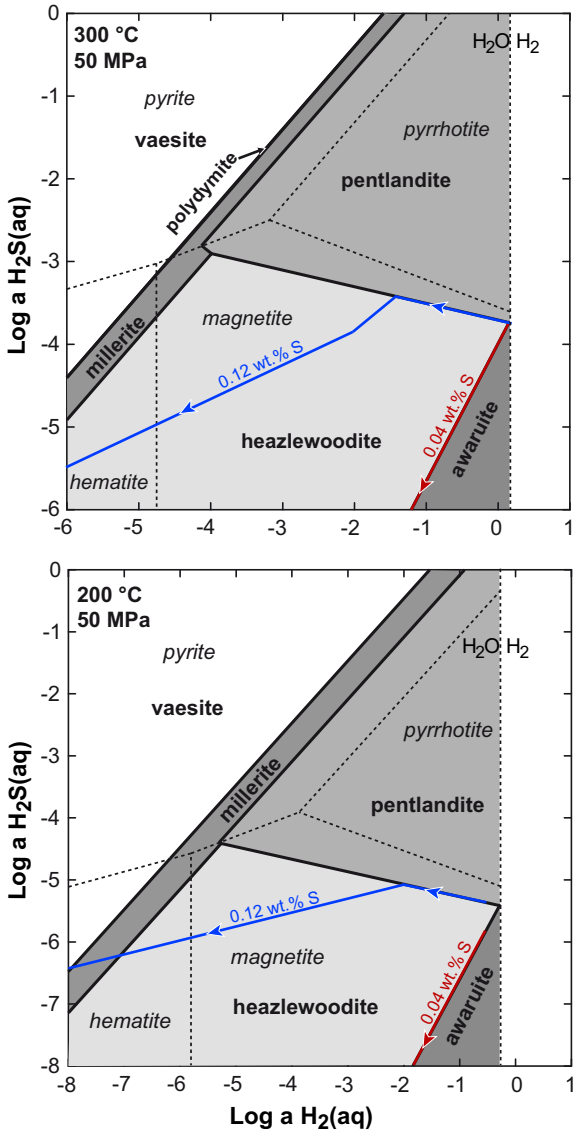

Fig. 8. Fe–Ni–O–S phase relations in H_2–H_2S activity diagrams. Shown are reaction paths for fluids with arrows pointing the direction of increasing water-to-rock ratios. Note the different paths taken for rock with low (0.04 wt.%) and high (0.12 wt.%) sulfur contents. Dashed lines are the boundaries of the magnetite, hematite, pyrrhotite and pyrite stability fields (field labels in italics); continuous lines are boundaries of awaruite, pentlandite, heazlewoodite, millerite, polydymite and vaesite stability fields (bold field labels). (For interpretation of the references to color in this figure, the reader is referred to the web version of this article.)

1274A, constraints on serpentinization temperatures are required.

Serpentinization temperatures have been estimated for rocks from Hole 1274A using phase relationships (Bach et al., 2004; Klein and Bach, 2009) and whole rock oxygen isotope compositions (Alt et al., 2007). Bach et al. (2004) interpret the replacement of olivine by serpentine, brucite and magnetite in the presence of fresh clinopyroxene from the upper half of Hole 1274A, to be indicative of low serpentinization temperatures, probably <200–250 °C. Based on the high $\delta^{18}O$ values (up to 8.1‰) of whole rocks from Hole 1274A, Alt et al. (2007) proposed low alteration temperatures (<150 °C). Klein and Bach (2009) found co-occurring iron–nickel- and cobalt–pentlandite endmembers in samples from Hole 1274A, which can coexist only at temperatures below ~200 °C (Kaneda et al., 1986). The serpentine and brucite compositions predicted for this temperature range are in a very good agreement with compositions of serpentine and brucite from Hole 1274A (Figs. 2–6).

The evaluation of predicted and measured mineral compositions in combination with temperature estimates mentioned above, allows us to approximate water-to-rock ratios during serpentinization (Figs. 2–6). At 150 °C the dunite and the harzburgite model predict a w/r of ~3 and ~4, respectively, for serpentine Mg# 95 and brucite Mg# 80. At 200 °C the corresponding w/r predicted by both models is ~1. Although these estimates are fairly rough, the numbers are similar to what has been approximated for the root zone of the Lost City hydrothermal system (Früh-Green et al., 2003; Foustoukos et al., 2008).

4.2. Changing Fe–Ni–O–S phase assemblages during serpentinization

We examine Fe–Ni–O–S phase equilibria with changing temperature and w/r ratio in Fig. 8. Phases of the Fe–Ni–O–S system provide a useful monitor for changing H_2 and H_2S activities during progressive serpentinization (Eckstrand, 1975; Frost, 1985; Alt and Shanks, 1998; Klein and Bach, 2009). Klein and Bach (2009) interpret the occurrence of pentlandite + awaruite + magnetite, the dominating Fe–Ni–O–S assemblage in partly serpentinized rocks from Hole 1274A, to be indicative of consistently reducing conditions prevailing throughout serpentinization. The occurrence of this mineral assemblage indicates that the system was near H_2 saturation and that a separate H_2-rich vapor phase may develop during serpentinization at low pressures. Moreover, at site 1274 awaruite was found only in samples containing abundant brucite. Our reaction path models corroborate these findings, as awaruite is predicted to form only where brucite is stable, i.e. below ~330 °C. Above these temperatures awaruite will not be stable as conditions are not sufficiently reducing. In addition, the modeling results underscore the relevance of $\sum S$ in the system in interpreting opaque phase relations (Fig. 8). Apart from redox conditions determined by equilibria in the $MgO–SiO_2–FeO–Fe_2O_3–H_2O$ system, the bulk sulfur content of the rock determines whether or not pentlandite will be part of the equilibrium assemblage at w/r ratios of 1 and above. Low $\sum S$ will cause pentlandite to desulfurize and the assemblage heazlewoodite + awaruite + magnetite to be stable (see Fig. 8, cf. Peretti et al., 1992). In contrast, if $\sum S$ is elevated, pentlandite will desulfurize only in part, even at highly reducing conditions. Yet higher $\sum S$ will hinder awaruite to form at the expense of pentlandite. Instead, pentlandite is predicted to coexist with heazlewoodite and magnetite. However, a direct correlation between $\sum S$ content of the rock and the presence (or lack) of heazlewoodite was not observed. The same holds true for the sulfur content of the serpentine matrix surrounding heazlewoodite

as no clear trend was observed. Perhaps heazlewoodite nucleation is overstepped, since it is found only in strongly to fully serpentinized peridotites (Klein and Bach, 2009). Overstepping of heazlewoodite formation would allow pentlandite + awaruite + magnetite to exist metastably at slightly less reducing conditions. If we account for metastable equilibrium of pentlandite + awaruite + magnetite and suppress the formation of heazlewoodite in our calculations to simulate overstepping of heazlewoodite nucleation, our model predicts that pentlandite is part of the equilibrium assemblage over the entire temperature range at w/r ~ 1, together with awaruite occurring at $T < 330$ °C.

4.3. Fe^{+2}–Fe^{+3} exchange equilibria in serpentinites

Evans (2008) reviewed the serpentinite literature focusing on the oxidation state of Fe and $Fe^{+2}Mg_{-1}$ exchange equilibria in serpentinites and emphasized the importance of Fe^{+3} in serpentine as it contributes to hydrogen formation during serpentinization. However, there is a lack of Fe^{+3}-data for abyssal serpentinites. O'Hanley and Dyar (1993) report Mößbauer results from Archean serpentinites that indicate (1) significant Fe^{+3} in serpentinite (about 50% of the total Fe) and (2) significant Fe^{+3} in tetrahedral sites, again about 50% (cf. Page, 1968; Whittaker and Wicks, 1970; Blaauw et al., 1979; Rozenson et al., 1979; González-Mancera et al., 2003). Our EMPA data reveal at least 1.97 mol of Si (on the basis of 7 oxygens) in the tetrahedral site of serpentine in mesh-rims. Additionally, aluminum accounts for up to 0.01 formula units in the tetrahedral site (see Table A1). Hence, in the tetrahedral site of serpentine with 0.15 mol of Fe (calculated as FeO) less than 0.02–0.03 mol per formula unit can be occupied by Fe^{+3}. This is equivalent to ~15–20% of the total iron. Mößbauer spectroscopy applied to separated mesh-rims of partly serpentinized dunites and harzburgites reveals the presence of significant amounts of Fe^{+3} in hydrous secondary minerals (Table 4). Trivalent Fe is present in both tetrahedral and octahedral sites, but occupies preferentially the octahedral site (48–86%, mean = 64% of total Fe^{+3}). This result is at least qualitatively in concert with results of EMPA. However, in the bastite sample Fe^{+3} occupies preferentially the tetrahedral site.

In mesh-rims of weakly serpentinized peridotites the $Fe^{+3}/\sum Fe$ ranges between 0.30 and 0.48. In mesh-rims of strongly to fully serpentinized peridotites the $Fe^{+3}/\sum Fe$ of hydrous secondary phases is between 0.53 and 0.68, which is considerably higher than in weakly serpentinized peridotites. The higher $Fe^{+3}/\sum Fe$ may be linked to decreased $a_{H_2,aq}$, either because the reducing capacity of the rock decreases or through diffusive/advective loss of H_2,aq (see (R7)) or both. Increasing $a_{SiO_2,aq}$ is unlikely to promote higher $Fe^{+3}/\sum Fe$ as $a_{SiO_2,aq}$ is buffered to exceedingly low values at low temperatures by (R9). We assume that the Fe^{+3} detected resides chiefly in serpentine, although uptake of Fe^{+3} by brucite cannot be excluded. In general, $Fe^{+3}/\sum Fe$-data obtained by Mößbauer spectroscopy represent an upper limit and must be interpreted with caution, because oxidation of ferrous iron in serpentine and brucite under atmospheric conditions during sample recovery and subsequent storage is possible. It is also possible that diffusive loss of hydrogen after serpentinization but before sampling leads to cryptic oxidation of serpentinites.

Between 150 and 250 °C (the expected temperature range of serpentinization at Hole 1274A (Bach et al., 2006; Alt et al., 2007; Klein and Bach, 2009) the predicted $Fe^{+3}/\sum Fe$ of serpentine appears largely insensitive to precursor rock mineralogy but varies significantly with changes in w/r ratio and temperature (Figs. 5 and 6). At 150 °C and w/r ~ 3, where brucite and serpentine have predicted compositions in accordance with natural equivalents from Hole 1274A (Mg# of brucite = 80 and Mg# of serpentine = 95), the $Fe^{+3}/\sum Fe$ is 0.33, i.e., comparable to the lowest $Fe^{+3}/\sum Fe$ measured in partly serpentinized peridotites (Table 4). At 200 °C and a w/r of 0.6, where predicted brucite and serpentine also have compositions in accordance with their natural equivalents, the predicted $Fe^{+3}/\sum Fe$ is 0.21, which is lower than what is measured in natural samples. However, because our calculations do not allow for iron partitioning into the tetrahedral sites, the predicted proportions of Fe^{+3} in serpentine have to be considered as minimal values. With increasing temperatures the mismatch between observation and prediction increases further, which is seen as evidence that serpentinization of rocks from Hole 1274A took place at temperatures below 250 °C and low w/r ratios.

4.4. Geochemical reaction path modeling and serpentinization experiments

Seyfried et al. (2007) conducted serpentinization experiments of a spinel–lherzolite at 200 °C and 50 MPa. They reported a Mg# of 91 and the $Fe^{+3}/\sum Fe$ of experimentally derived hydrous alteration products, i.e., serpentine is ~0.42 and thus consistent with $Fe^{+3}/\sum Fe$ of serpentine of partly serpentinized peridotites from Hole 1274A. To compare their experimental results with our geochemical reaction path modeling results we have to know the exact w/r, where w/r is mass of water divided by mass of solids. Seyfried et al. (2007) started their experiment with 44 g artificial seawater and 40 g spinel–lherzolite. In the course of their experiment about 55 wt.% of the solid starting material (equivalent to 22 g of rock) reacted to serpentine and brucite, thus the final w/r was ~2. The calculated $Fe^{+3}/\sum Fe$ of serpentine from our olivine (2A) and harzburgite (2B) models is 0.3 at w/r ~ 2. The difference between the calculated and the experimentally derived $Fe^{+3}/\sum Fe$ values (0.42) can be due to (1) incorporation of ferric iron in brucite, (2) incorporation of Fe^{+3} in the tetrahedral site of serpentine, or (3) weaknesses of the thermodynamic data and solid solution models. Another factor is that the models represent equilibrium conditions and it is evident that equilibrium was not achieved in the experiments. Overall, the model prediction of significant uptake of Fe^{+3} into serpentine is consistent with experimental and observational data. The lack of magnetite in the experiments by Seyfried et al. (2007) is not matched by our predictions for 200 °C and w/r = 2. Our models predict, however, that magnetite may not form at temperatures below 150 °C and w/r < 1. This result may indicate that the thermodynamic drive for

magnetite formation in the 200 °C experiments was fairly small, perhaps too small to allow magnetite to nucleate.

Dihydrogen concentrations were up to 77 mM in the experiments of Seyfried et al. (2007), which is more than four times lower than what these authors predicted in a geochemical reaction path model (350 mM) that emulates the serpentinization of a lherzolite (62 vol.% Ol, 26 vol.% Opx, 10 vol.% Cpx, 2 vol.% Sp), while ignoring solid solutions. McCollom and Bach (2009) emphasize that the partitioning of Fe between secondary minerals will exert a strong influence on the amount of H_2,aq generated during serpentinization. The large difference between predicted and observed H_2,aq concentration is likely related to the lack of serpentine and brucite solid solutions in the reaction path model of Seyfried et al. (2007) (i.e., Fe is not allowed to be incorporated in serpentine and brucite). McCollom and Bach (2009) and this study show that the partitioning of Fe into serpentine and brucite demonstrated experimentally (Moody, 1976; Seyfried et al., 2007) can be matched at least semi-quantitatively in reaction path models that allow solid solutions to form. This is a crucial step forward in increasing the reliability of predictions of hydrogen yields during serpentinization.

Our serpentinization model of olivine (Model 2A) predicts a concentration of 82 mM at 200 °C at a w/r of 2. In the corresponding serpentinization model of harzburgite (Model 2B) the predicted H_2,aq concentration is 94 mM. Like in the calculations by McCollom and Bach (2009), these concentrations are similar to those measured by Seyfried et al. (2007; 77 mM). The match in H_2,aq concentrations is noteworthy, because the mineral proportions used in the experiments and model calculation are different. It appears that regardless of peridotite composition, serpentinization at a temperature of 200 °C, a pressure of 50 MPa and a w/r $\sim$ 2 cannot yield more than about 100 mM H_2,aq. An obvious explanation for this phenomenon is that all compositions used have serpentine–brucite–magnetite phase relations that govern the H_2 activities. If a rock composition is chosen that has other stable mineral assemblage at 200 °C, i.e., serpentine–talc–magnetite, the hydrogen fugacities are expected to be much lower, as a higher silica activity would stabilize Fe in serpentine [$Fe_3Si_2O_5(OH)_4 = Fe_3O_4 + 2SiO_2$,aq + H_2O + H_2 (cf. Frost and Beard 2007)].

Allen and Seyfried (2003) conducted serpentinization experiments of olivine (Mg# 89) at 400 °C and 50 MPa to better assess alteration and mass transfer in high temperature ultramafic-hosted hydrothermal systems. We used their experimentally determined fluid compositions to check consistency with predictions of our serpentinization Model 1A (see Fig. 6). Predicted and measured concentrations of dissolved Mg (predicted 39 mM; measured 27 mM), Si (1.1 mM; 0.2 mM), Fe (5.5 mM; 13.3 mM), Ca (0.3 mM; 0.3 mM) and H_2,aq (1.3 mM; 1.2 mM) are in general agreement (see Fig. 5), although Allen and Seyfried (2003) used artificial seawater with high concentrations of Cl and Na to simulate fluids emanating from the Rainbow hydrothermal field. Moreover, the measured pH (at 25 °C) of 5.27, equivalent to an in situ pH of 4.9 is in close agreement with our predicted in situ pH of 4.8. Consistent with the model calculations, the experiment by Allen and Seyfried (2003) shows unambiguously that olivine is almost unreactive at temperatures of 400 °C and pressures of 50 MPa.

Berndt et al. (1996) conducted a serpentinization experiment of olivine (Mg# 88) at 300 °C and 50 MPa. The observed alteration mineralogy consists of Fe-poor serpentine, brucite and magnetite, which is in agreement with our modeling results (see Fig. 6, serpentine Mg# 97; brucite Mg# 93). However, at w/r $\sim$ 2 their analyzed fluid composition is clearly at odds with our predictions, which can be explained with the fact that they used a starting fluid containing almost no dissolved cations besides Na. Nevertheless, concentrations of Si (predicted 21 μM; measured 31 μM) and H_2,aq (146 versus 158 mM) are very similar, indicating buffering by serpentine, brucite and magnetite (Figs. 6 and 7). In a similar experiment by Janecky and Seyfried (1986), where a synthetic dunite was reacted with artificial seawater (equivalent to seawater that we used in our models) at 300 °C, 50 MPa and a w/r $\sim$ 10, concentrations of dissolved elements are in agreement with our predictions. The concentration of H_2 was not determined during their experiment, so comparison with the model predictions is not possible.

In spite of the limitations, the results of thermodynamic reaction path modeling are, at least semi-quantitatively, in a very good agreement with experimental results, underscoring the relevance of solid solutions in geochemical reaction path models for the interpretation of mineral–fluid equilibria during serpentinization. While these models have increased predictive power, the results should be regarded provisional, until experimentally derived thermodynamic data for serpentine and brucite solid solutions exist.

4.5. The formation of brucite and serpentine in mesh-rims

Independent of the extent of serpentinization, mesh-rims exhibit a distinct zoning starting with brucite at the interface with olivine to a zone of α-serpentine + brucite ± magnetite and finally serpentine and magnetite at the outer rim (Figs. 1, 2 and 4). The reaction path models that provide phase equilibria changes in the system MgO–SiO_2–FeO–Fe_2O_3–H_2O on a sliding scale of water-to-rock ratios do not predict the observed mineral zoning. The temperature interval during which olivine–serpentine and brucite coexist stably is extremely narrow, so that the presence of iron does not change significantly the invariant nature of the iron-free system (cf. Trommsdorff and Evans, 1972).

Equilibria between olivine, serpentine and brucite in the MgO–SiO_2–H_2O system are governed by the following reactions (see Fig. 9):

$$\underset{\text{olivine}}{3Mg_2SiO_4} + SiO_2,\text{aq} + 4H_2O = \underset{\text{serpentine}}{2Mg_3Si_2O_5(OH)_4}. \quad \text{(R12)}$$

$$\underset{\text{olivine}}{2Mg_2SiO_4} + 3H_2O = \underset{\text{serpentine}}{Mg_3Si_2O_5(OH)_4} + \underset{\text{brucite}}{Mg(OH)_2}. \quad \text{(R13)}$$

$$\underset{\text{olivine}}{Mg_2SiO_4} + 2H_2O = SiO_2,\text{aq} + \underset{\text{brucite}}{2Mg(OH)_2}. \quad \text{(R14)}$$

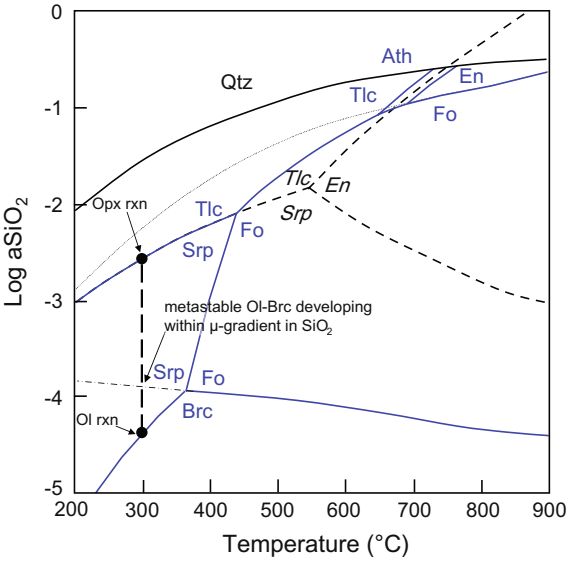

Fig. 9. Temperature–SiO_2 activity plot depicting the phase relations in the system MgO–SiO_2–H_2O. Note the pressure is 200 MPa to allow for calculation of phase boundaries at temperatures >400 °C. Thick lines are stable phase boundaries, while thin and dashed lines are metastable ones. Mineral abbreviations are after Kretz (1983). See text for discussion. (For interpretation of the references to color in this figure, the reader is referred to the web version of this article.)

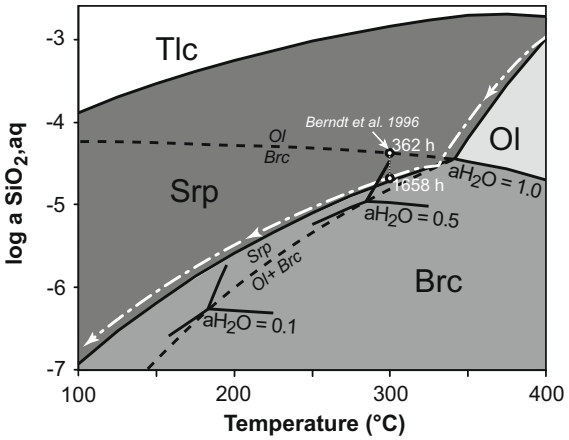

Fig. 10. Temperature–SiO_2 activity plot showing in the phase relations during olivine breakdown in greater detail than Fig. 9. Solid lines show stable phase boundaries. Black dashed lines show metastable phase boundaries. White dashed line denotes the $a_{SiO_2,aq}$ path of Model 1A. Polythermal olivine–serpentine–brucite equilibrium is possible if $a_{H_2O} < 1$. Also shown is the range of silica observed in experiments from Berndt et al. (1996). See text for discussion.

Above ~330 °C, olivine should be converted to serpentine following (R12). If there is no external source of silica (e.g., from orthopyroxene breakdown), this reaction is not expected to yield much serpentine. Also, olivine shows brucite – not serpentine – at the reaction front, so we rule out (R12) from having played a large role in serpentinization of rocks from Hole 1274A. Reaction (R13) represents the invariant point at $a_{H_2O} \sim 1$ and $T < \sim 330$ °C at which olivine should react instantaneously to form serpentine and brucite.

There are a number of possibilities that can explain the coexistence of olivine, serpentine, brucite and a fluid. One is non-unity activity of water (Sanford, 1981), because the system gains a degree of freedom if $p_{H_2O} < p_{total}$, allowing for univariant four phase equilibria in the MgO–SiO_2–H_2O system (Fig. 10). Indeed, the water activity may be reduced near the serpentinization front, where water is consumed. Enrichment of chlorine near the reaction front would be expected (e.g., Sanford, 1981) but this is not observed in rocks from Hole 1274A. Also, the brucite zone between olivine and serpentine is at odds with olivine–serpentine–brucite equilibrium, as serpentine and olivine are physically separated by brucite.

It seems therefore more likely that metastable equilibria between olivine, serpentine and brucite or arrested reactions in olivine serpentinization need to be considered to explain the brucite rims. Reaction (R13) can be broken down in two sub-reactions (R14) and (R9), which can be taken into consideration to explain the zoning in the mesh-rims. If (R14) took place, silica activity would increase, the fluid would move into the serpentine stability field, and serpentine may ultimately form once the Gibbs energy required for its nucleation is available. In this sense, the brucite rims may represent an arrested reaction. While brucite prevails at the frozen reaction front, the outer mesh-rims lack brucite entirely. This is best explained by the strong contrast in silica activities developing locally within a peridotite undergoing serpentinization (Fig. 9). When metastable orthopyroxene reacts at $T < 400$ °C, it is expected to form serpentine and talc. The associated inter-granular fluid will have a relatively high silica activity. In contrast, serpentine + brucite forming from olivine breakdown reactions will impose very low silica activities on the intergranular fluid. It is likely that this strong gradient in silica activity (Fig. 9) can lead to diffusive silica transport between orthopyroxene and olivine. Interestingly, the metastable olivine–brucite phase boundary is situated between the talc–serpentine and brucite–serpentine buffers (Fig. 9). Perhaps the system dwells in this metastable state near the contact with olivine, but away from it, silica released from orthopyroxene breakdown provides enough excess thermodynamic drive to form serpentine.

Experimental data may help to shed some light on this issue. The only experiment for which silica data are available throughout the runtime of the experiment is that of Berndt et al. (1996). These authors conducted serpentinization experiments with pure olivine (Mg# 88) as the starting material and found that replacement products were Fe-poor serpentine, brucite and magnetite. Again, assuming full equilibrium at 300 °C (and at $a_{H_2O} = 1$) olivine should react to form contemporaneously serpentine and brucite, which is in accordance with their findings and our modeling results. In the course of the experiment, however, silica

first increased and subsequently decreased. Fig. 10 illustrates the isothermal reaction path of SiO_2. which starts between the stable univariant phase boundary of (R9) and the metastable branch of (R14). Concentrations of SiO_2 increase until (at 362 h reaction progress) a maximum is reached, which matches the metastable branch of (R14). Subsequently the concentration of SiO_2 drops until it reaches the univariant phase boundary of (R9) (at 1658 h). This experimental reaction path may be taken as evidence for (R14) taking place before (R9), which will ultimately control the SiO_2 activity of the entire system when olivine is exhausted. More serpentinization experiments and sufficiently accurate SiO_2,aq analyses are needed to constrain this further.

5. CONCLUSIONS

Our study indicates that unprecedented details about the reaction sequences during serpentinization may be obtained from merging careful petrographic, mineral chemical, magnetic and Mößbauer spectroscopic analyses with comprehensive thermodynamic modeling. We have calculated how dihydrogen generation depends on temperature, rock composition and fluid/rock ratios during serpentinization. Below 320–330 °C it is entirely controlled by serpentine–magnetite–brucite equilibria. We have specifically addressed the partitioning of divalent iron into brucite and divalent as well as trivalent iron into serpentine.

Model calculations reveal that both partitioning and oxidation state of iron are very sensitive to temperature and water-to-rock ratio during serpentinization. As the compositions of coexisting serpentine (Mg# 95) and brucite (Mg# 80) are almost constant in most samples from Hole 1274, it is likely that alteration conditions were very similar downhole. Based on our modeling results, we propose serpentine and brucite formation temperatures ranging from <150 to 250 °C. Corresponding bulk water-to-rock ratios range from <0.1 to 5. Awaruite must have formed during main stage serpentinization at temperatures between 200 and 250 °C and $w/r < 1$, when hydrogen fugacities are maximal.

Rock composition appears to be of key importance for our understanding of Fe-partitioning during serpentinization. Serpentinization of orthopyroxene generates more dihydrogen than serpentinization of olivine at high temperatures (>330 °C). This is the case because olivine breakdown to serpentine and magnetite depends on the availability of an external silica source. At temperatures below 330 °C brucite is stable and an external silica source is no longer required to facilitate the formation serpentine and magnetite. Accordingly, dihydrogen concentration peaks approximately at 320–330 °C (depending on protolith mineralogy) when brucite emerges. In the temperature range where brucite is present, the dihydrogen yield by serpentinization of olivine will exceed by far the dihydrogen yield by serpentinization of orthopyroxene.

A significant amount of divalent iron partitions into brucite and does not drive dihydrogen generation. Textural evidence indicates that olivine is replaced by brucite (and not serpentine) along the grain boundaries so that the formation of brucite appears to be the initial step of a serpentinization reaction sequence. We propose that brucite is metastable in the stability field of serpentine until enough thermodynamic drive for serpentine nucleation is available.

The formation of Fe^{+3}-serpentine markedly contributes to hydrogen generation, in particular at low temperatures and low water-to-rock ratios. Mößbauer spectroscopic results indicate that about 30–50% of the iron in serpentine/brucite mesh-rims is trivalent, irrespective of subbasement depth and the orthopyroxene content of the precursor rock. Our geochemical reaction path models are semi-quantitatively in agreement with the spectroscopic results if serpentinization temperatures were 150 to 250 °C.

If the Fe^{+3}-component of serpentine is neglected in geochemical reaction path models, magnetite is predicted to be part of the equilibrium assemblage over the entire temperature range. In contrast, if Fe^{+3} is allowed to partition into serpentine, magnetite is not predicted to form at $T < 150$–200 °C. Consistent with this notion, in a recent experimental study Seyfried et al. (2007) reported on the lack of magnetite formation during serpentinization of peridotite at 200 °C. This result underscores the importance of considering the Fe^{+3}-component in serpentine solid solution models. However, since Fe^{+3} was not allowed to substitute for silicon in tetrahedral coordination in the present study, our modeling results should be regarded as provisional. To improve the predictive power of serpentinization models, experimentally derived thermodynamic data of Fe^{+3}-serpentine and thermodynamic parameters for the serpentine solid solution are necessary.

ACKNOWLEDGMENTS

The authors thank Michael Hentscher for his help in setting up the thermodynamic database. Many thanks go to Ron Frost for inspiring and stimulating discussions. James Beard, Dionysis Foustoukos and Ivan Savov are thanked for helpful and critical reviews. Jeff Alt is thanked for the editorial handling. We thank Barbara Mader and Peter Appel for their assistance with the electron microprobe analyses. Carlos Garrido and Holger Paulick provided sample material and thin sections. We used samples supplied by the Ocean Drilling Program (ODP). ODP is sponsored by the US National Science Foundation (NSF) and participating countries under management of Joint Oceanographic Institutions (JOI), Inc. This work was supported with funds from the Special Priority Program 1144 of the German Science Foundation (BA 1605/1-1 and BA 1605/1-2) and by the DFG-Research Center/Excellence Cluster 'The Ocean in the Earth System'. This is publication No. 40 of the Priority Program 1144 "From Mantle to Ocean: Energy-, Material- and Life-cycles at Spreading Axes". The Institute for Rock Magnetism (IRM) is funded by the Instrumentation and Facilities program of the Earth Science Division of NSF (NSF/EAR0732473), the W. M. Keck Foundation and University of Minnesota. This is IRM publication No. 0901.

APPENDIX A

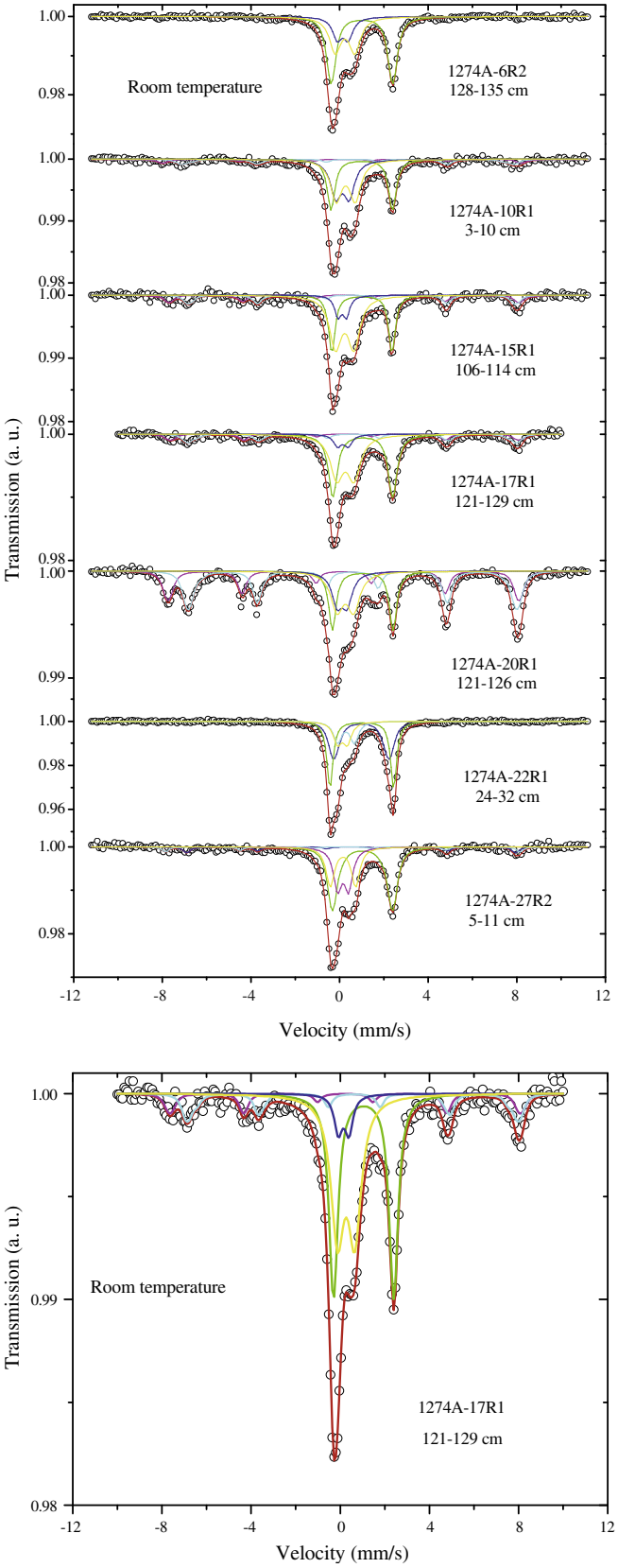

Fig. A1. Mößbauer spectra at room temperature. Open circles are experimental points and red line is the best fitting (magenta, magnetite site A; light blue, magnetite site B; green, Fe^{+2}; dark blue, Fe^{+3} tetrahedral; yellow, Fe^{+3} octahedral). (For interpretation of the references to color in this figure legend, the reader is referred to the web version of this article.)

Table A1
Selected electron microprobe analyses.

Hole	1274A	1274A	1274A	1274A	1274A	1274A	1274A	1274A	1274A	1274A	1274A	1274A
Core	4	6	10	17	22	27	4	6	10	17	22	27
Section	1	2	1	1	1	2	1	2	1	1	1	2
Depth (cm)	104–105	128–135	3–10	121–129	24–32	5–11	104–105	128–135	3–10	121–129	24–32	5–11
Depth (mbsf)	22.79	32.78	49.33	89.51	122.34	147.65	22.79	32.78	49.33	89.51	122.34	147.65
Rock type	Hz	Hz	Du	Hz	Hz	Hz	Hz	Hz	Du	Hz	Hz	Hz
Lab code	None	Ap-86	AP-88	AP-95	AP-99	AP-103	None	AP-86	AP-88	AP-95	AP-99	AP-103
Mineral	Ol	Ol	Ol	Ol	Ol	Ol	Srp	Srp	Srp	Srp	Srp	Srp
Texture	Mesh	Mesh	Mesh	Mesh	Mesh	Mesh	Mesh	Mesh	Mesh	Mesh	Mesh	Mesh
Wt.%												
SiO_2	40.84	40.73	40.85	41.10	40.87	40.31	39.72	40.76	40.91	40.70	40.58	39.95
TiO_2	0.02	0.02	0.00	0.00	0.03	0.03	0.01	0.03	0.01	0.01	0.05	0.03
Al_2O_3	0.04	0.03	0.03	0.04	0.02	0.02	0.28	0.11	0.08	0.17	0.09	0.26
Cr_2O_3	0.01	0.01	0.01	0.02	0.02	0.02	0.00	0.04	0.03	0.02	0.00	0.02
FeO	8.14	8.27	8.26	8.18	7.67	8.20	4.00	4.28	4.20	3.08	4.23	3.45
MnO	0.11	0.12	0.11	0.13	0.09	0.10	0.06	0.08	0.10	0.08	0.09	0.09
MgO	50.22	49.89	50.26	49.86	50.70	50.73	37.70	38.69	39.44	39.58	38.45	39.05
NiO	0.38	0.37	0.38	0.38	0.41	0.40	0.30	0.32	0.42	0.46	0.27	0.40
CoO	0.03	0.04	0.02	0.01	0.03	0.02	0.01	0.02	0.02	0.01	0.02	0.01
SO_3	0.00	0.00	0.02	0.00	0.01	0.01	0.13	0.06	0.05	0.13	0.04	0.10
CaO	0.07	0.09	0.25	0.07	0.03	0.06	0.06	0.08	0.10	0.05	0.04	0.06
Na_2O	0.02	0.02	0.00	0.00	0.00	0.00	0.03	0.03	0.00	0.00	0.01	0.02
	0.00	0.00	0.00	0.00	0.00	0.00	0.01	0.00	0.00	0.00	0.00	0.01
Total	99.88	99.59	100.19	99.79	99.88	99.90	82.31	84.50	85.36	84.29	83.87	83.45
Formula												
Si	1.00	1.00	0.99	1.00	0.99	0.99	1.99	1.99	1.98	1.98	1.99	1.97
Ti	0.00	0.00	0.00	0.00	0.00	0.00	0.00	0.00	0.00	0.00	0.00	0.00
Al	0.00	0.00	0.00	0.00	0.00	0.00	0.01	0.00	0.00	0.00	0.00	0.01
Cr	0.00	0.00	0.00	0.00	0.00	0.00	0.00	0.00	0.00	0.00	0.00	0.00
Fe	0.17	0.17	0.17	0.17	0.16	0.17	0.17	0.17	0.17	0.13	0.17	0.14
Mn	0.00	0.00	0.00	0.00	0.00	0.00	0.00	0.00	0.00	0.00	0.00	0.00
Mg	1.83	1.82	1.82	1.81	1.84	1.85	2.81	2.81	2.84	2.87	2.81	2.87
Ni	0.01	0.01	0.01	0.01	0.01	0.01	0.01	0.01	0.02	0.02	0.01	0.02
Co	0.00	0.00	0.00	0.00	0.00	0.00	0.00	0.00	0.00	0.00	0.00	0.00
S	0.00	0.00	0.00	0.00	0.00	0.00	0.00	0.00	0.00	0.00	0.00	0.00
Ca	0.00	0.00	0.01	0.00	0.00	0.00	0.00	0.00	0.01	0.00	0.00	0.00
Na	0.00	0.00	0.00	0.00	0.00	0.00	0.00	0.00	0.00	0.00	0.00	0.00
K	0.00	0.00	0.00	0.00	0.00	0.00	0.00	0.00	0.00	0.00	0.00	0.00
Total	3.01	3.00	3.00	2.99	3.01	3.02	4.99	4.98	5.02	5.00	4.98	5.01
Oxygens	4	4	4	4	4	4	7	7	7	7	7	7

Hole	1274A	1274A	1274A	1274A	1274A	1274A
Core	4	6	10	17	22	27
Section	1	2	1	1	1	2
Depth (cm)	104–105	128–135	3–10	121–129	24–32	5–11
Depth (mbsf)	22.79	32.78	49.33	89.51	122.34	147.65
Rock type	Hz	Hz	Du	Hz	Hz	Hz
Lab code	None	AP-86	AP-88	AP-95	AP-99	AP-103
Mineral	Brc	Brc	Brc	Brc	Brc	Brc
Texture	Mesh	Mesh	Mesh	Mesh	Mesh	Mesh
Wt.%						
SiO_2	1.27	0.93	1.18	17.26	0.56	0.86
TiO_2	0.02	0.01	0.00	0.00	0.00	0.00
Al_2O_3	0.71	0.41	0.08	0.40	0.22	0.68
Cr_2O_3	0.01	0.00	0.00	0.01	0.00	0.00
FeO	28.31	21.75	20.34	17.66	21.20	17.80
MnO	0.77	0.94	0.64	0.48	0.64	0.74
MgO	38.35	48.18	49.37	43.84	49.26	50.37
NiO	0.76	1.88	0.51	0.67	0.44	0.59
CoO	0.10	0.06	0.04	0.05	0.05	0.05

(*continued on next page*)

Table A1 (*continued*)

SO_3	0.42	0.18	0.18	0.40	0.10	0.13
CaO	0.07	0.29	0.24	0.12	0.14	0.30
Na_2O	0.03	0.00	0.02	0.03	0.05	0.01
K_2O	0.00	0.00	0.00	0.00	0.01	0.01
Total	70.82	74.63	72.60	80.92	72.67	71.54
Formula						
Si	0.01	0.01	0.01	0.15	0.01	0.01
Ti	0.00	0.00	0.00	0.00	0.00	0.00
Al	0.00	0.00	0.00	0.00	0.00	0.00
Cr	0.00	0.00	0.00	0.00	0.00	0.00
Fe	0.27	0.19	0.18	0.13	0.19	0.16
Mn	0.01	0.01	0.01	0.00	0.01	0.01
Mg	0.66	0.75	0.78	0.56	0.78	0.80
Ni	0.01	0.02	0.00	0.00	0.00	0.01
Co	0.00	0.00	0.00	0.00	0.00	0.00
S	0.00	0.00	0.00	0.00	0.00	0.00
Ca	0.00	0.00	0.00	0.00	0.00	0.00
Na	0.00	0.00	0.00	0.00	0.00	0.00
K	0.00	0.00	0.00	0.00	0.00	0.00
Total	0.96	0.98	0.98	0.84	0.99	0.99
Oxygens	1	1	1	1	1	1
Calc. endm. Mg#	63.4	78.6	79.7	71.7	80.7	81.5
# Analyses	68	114	194	149	84	28
R^2	0.84	0.83	0.96	0.89	0.87	0.84

Hole	1274A	1274A	1274A	1274A	1274A	1274A	1274A	1274A	1274A	1274A	1274A
Core	4	6	17	22	27	4	6	10	17	22	27
Section	1	2	1	1	2	1	2	1	1	1	2
Depth (cm)	104–105	128–135	121–129	24–32	5–11	104–105	128–135	3–10	121–129	24–32	5–11
Depth (mbsf)	22.79	32.78	89.51	122.34	147.65	22.79	32.78	49.33	89.51	122.34	147.65
Rock type	Hz	Hz	Hz	Hz	Hz	Hz	Hz	Du	Hz	Hz	Hz
Lab code	None	AP-86	AP-95	AP-99	AP-103	None	AP-86	AP-88	AP-95	AP-99	AP-103
Mineral	Opx	Opx	Opx	Opx	Opx	Srp	Srp	Srp	Srp	Srp	Srp
Texture	Bastite	Bastite	Bastite	Bastite	Bastite	Bastite	Bastite	Bastite	Bastite	Bastite	Bastite
Wt.%											
SiO_2	55.65	56.10	56.74	55.93	55.15	37.64	37.99	34.90	40.81	39.10	39.12
TiO_2	0.02	0.03	0.04	0.01	0.03	0.03	0.01	0.02	0.02	0.03	0.05
Al_2O_3	3.00	2.67	2.36	2.52	2.60	1.95	1.54	1.75	1.55	1.38	1.73
Cr_2O_3	0.89	0.89	0.77	0.97	0.89	0.93	0.86	1.39	0.94	0.94	0.94
FeO	5.19	5.26	4.95	4.86	5.17	5.97	7.16	2.79	4.98	5.51	5.62
MnO	0.14	0.13	0.15	0.14	0.13	0.16	0.19	0.15	0.17	0.13	0.15
MgO	33.55	32.82	32.69	34.06	32.61	34.30	33.65	32.59	33.71	35.48	35.03
NiO	0.10	0.09	0.10	0.10	0.09	0.12	0.10	0.07	0.10	0.11	0.10
CoO	0.01	0.01	0.02	0.01	0.01	0.01	0.02	0.01	0.01	0.01	0.01
SO_3	0.01	0.01	0.02	0.00	0.01	0.16	0.09	0.31	0.12	0.16	0.23
CaO	1.64	1.46	2.08	1.33	1.29	0.88	0.66	0.10	1.79	0.10	0.66
Na_2O	0.02	0.02	0.03	0.06	0.04	0.04	0.04	0.02	0.03	0.02	0.03
K_2O	0.00	0.00	0.00	0.00	0.01	0.00	0.01	0.00	0.00	0.00	0.00
Total	100.22	99.49	99.95	99.99	98.03	82.19	82.32	74.10	84.23	82.97	83.67
Formula											
Si	0.98	0.99	0.99	0.98	0.99	1.95	1.97	1.98	2.02	1.98	1.97
Ti	0.00	0.00	0.00	0.00	0.00	0.00	0.00	0.00	0.00	0.00	0.00
Al	0.03	0.03	0.02	0.03	0.03	0.06	0.05	0.06	0.05	0.04	0.05
Cr	0.01	0.01	0.01	0.01	0.01	0.02	0.02	0.00	0.02	0.02	0.02
Fe	0.08	0.08	0.07	0.07	0.08	0.26	0.31	0.13	0.21	0.23	0.24
Mn	0.00	0.00	0.00	0.00	0.00	0.01	0.01	0.01	0.01	0.01	0.01
Mg	0.88	0.86	0.85	0.89	0.87	2.65	2.60	2.75	2.49	2.68	2.63
Ni	0.00	0.00	0.00	0.00	0.00	0.00	0.00	0.00	0.00	0.00	0.00
Co	0.00	0.00	0.00	0.00	0.00	0.00	0.00	0.00	0.00	0.00	0.00
S	0.00	0.00	0.00	0.00	0.00	0.01	0.00	0.01	0.00	0.01	0.01
Ca	0.03	0.03	0.05	0.03	0.02	0.05	0.04	0.01	0.13	0.01	0.04

Table A1 (*continued*)

Na	0.00	0.00	0.00	0.00	0.00	0.00	0.00	0.00	0.00	0.00	0.00
K	0.00	0.00	0.00	0.00	0.00	0.00	0.00	0.00	0.00	0.00	0.00
Total	2.01	2.00	1.99	2.01	2.00	5.01	5.00	4.95	4.93	4.98	4.97
Oxygens	6	6	6	6	6	7	7	7	7	7	7

Depth (cm), sample depth in core section; mbsf, meters below seafloor; Hz, harzburgite; Du, dunite; Ol, olivine; Opx, orthopyroxene; Srp, serpentine; Brc, brucite; Calc. endm. Mg#, calculated endmember brucite Mg#.

REFERENCES

Allen D. E. and Seyfried W. E. J. (2003) Compositional controls on vent fluids from ultramafic-hosted hydrothermal systems at mid-ocean ridges: an experimental study at 400 °C, 500 bars. *Geochim. Cosmochim. Acta* **67**, 1531–1542.

Alt J. C. and Shanks W. C. (1998) Sulfur in serpentinized oceanic peridotites: serpentinization processes and microbial sulfate reduction. *J. Geophys. Res.* **103**, 9917–9929.

Alt J. C., Shanks, III, W. C., Bach W., Paulick H., Garrido C. J. and Beaudoin G. (2007) Hydrothermal alteration and microbial sulfate reduction in peridotite and gabbro exposed by detachment faulting at the Mid-Atlantic Ridge, 15°20'N (ODP Leg 209): a sulfur and oxygen isotope study. *Geochem. Geophys. Geosyst.* **8**, Q08002. doi:10.1029/02007GC001617.

Armstrong J. T. (1995) CITZAF: a package of correction programs for the quantitative electron microbeam X-ray analysis of thick polished materials, thin films, and particles. *Microbeam Anal.* **4**, 177–200.

Bach W., Garrido C. J., Harvey J., Paulick H. and Rosner M. (2004) Variable seawater–peridotite interactions – first insights from ODP Leg 209, MAR 15°N. *Geochem. Geophys. Geosyst.* **5**, Q09F26. doi:10.1029/2004GC000744.

Bach W., Paulick H., Garrido C. J., Ildefonse B., Meurer W. P. and Humphris S. E. (2006) Unraveling the sequence of serpentinization reactions: petrography, mineral chemistry, and petrophyscis of serpentinites from MAR 15°N (ODP Leg 209, Site 1274). *Geophys. Res. Lett.* **33**, L13306. doi:10.1029/12006GL025681.

Beard J. S., Frost B. R., Fryer P., McCaig A., Searle R., Ildefonse B., Zinin P. and Sharma S. K. (2009) Onset and progression of serpentinization and magnetite formation in olivine-rich troctolite from IODP Hole U1309D. *J. Petrol.* **50**, 387–403.

Berman R. G., Engi M., Greenwood H. J. and Brown T. H. (1986) Derivation of internally-consistent thermodynamic data by the technique of mathematical programming: a review with application to the system MgO–SiO_2–H_2O. *J. Petrol.* **27**, 1331–1364.

Berndt M. E., Allen D. E. and Seyfried W. E. (1996) Reduction of CO_2 during serpentinization of olivine at 300 °C and 500 bars. *Geology* **24**, 351–354.

Blaauw C., Stroink G., Leiper W. and Zentilli M. (1979) Mössbauer analysis of some Canadian chrysotiles. *Can. Mineral.* **17**, 713–717.

Brand R. A. (1987) *NORMOS Programs. Internal Report*. Angewandte Physik, Universität Duisburg.

Cannat M. (1993) Emplacement of mantle rocks in the seafloor at mid-ocean ridges. *J. Geophys. Res.* **98**, 4163–4172.

Cannat M., Bideau B. and Bougault H. (1992) Serpentinized peridotites and gabbros in the Mid-Atlantic Ridge axial valley at 15°37'N and 16°52'N. *Earth Planet. Sci. Lett.* **109**, 87–106.

Chamberlain J. A., McLeod C. R., Traill R. J. and Lachance G. R. (1965) Native metals in the Muskox intrusion. *Can. J. Earth Sci.* **2**, 188–215.

Charlou J.-. L., Donval J.-. P., Fouquet Y., Jean-Baptiste P. and Holm N. (2002) Geochemistry of high H_2 and CH_4 vent fluids issuing from ultramafic rocks at the Rainbow hydrothermal field (36°14'N, MAR). *Chem. Geol.* **191**, 345–359.

Chase, Jr., M. W. (1998) NIST-JANAF Thermochemical Tables. In *J. Phys. Chem. Ref. Data Monograph No.* 9 (fourth ed.). American Institute of Physics, Woodbury, NY (also available on <http://webbook.nist.gov/>).

Chermak J. A. and Rimstidt J. D. (1989) Estimating the thermodynamic properties (ΔG°_f and ΔH°_f) of silicate minerals at 298 K from the sum of polyhedral contributions. *Am. Mineral.* **74**, 1023–1031.

D'Antonio M. and Kristensen M. B. (2004) Serpentine and brucite of ultramafic clasts from the South Chamorro Seamount (Ocean Drilling Program Leg 195, Site 1200): inferences for the serpentinization of the Mariana forearc mantle. *Min. Mag.* **68**, 887–904.

Dick H. J. B. (1989) Abyssal peridotites, very slow spreading ridges and ocean ridge magmatism. In *Magmatism in the Ocean Basins* (eds. A. D. Saunders and M. J. Norry), Geol. Soc. London, Spec. Pub. 42, pp. 71–105.

Douville E., Charlou J. L., Oelkers E. H., Bianvenu P., Jove Colon C. F., Donval J. P., Fouquet Y., Prieur D. and Appriou P. (2002) The Rainbow vent fluids (36°14'N, MAR): the influence of ultramafic rocks and phase separation on trace metal contents on Mid-Atlantic Ridge hydrothermal fluids. *Chem. Geol.* **184**, 37–48.

Drummond, Jr., S. E. (1981) Boiling and Mixing of Hydrothermal Fluids: Chemical Effects on Mineral Precipitation. Ph.D. thesis, Pennsylvania State University.

Eckstrand O. R. (1975) The Dumont Serpentinite: a model for control of nickeliferous opaque mineral assemblages by alteration reactions in ultramafic rocks. *Econ. Geol.* **70**, 183–201.

Escartín J., Hirth G. and Evans B. (1997) Effects of serpentinization on the lithospheric strength and the style of normal faulting at slow-spreading ridges. *Earth Planet. Sci. Lett.* **151**, 181–189.

Evans B. W. (2004) The serpentine multisystem revisited: chrysotile is metastable. *Int. Geol. Rev.* **46**, 479–506.

Evans B. W. (2008) Control of the products of serpentinization by the $Fe^{2+}Mg_{-1}$ exchange potential of olivine and orthopyroxene. *J. Petrol.* **49**, 1873–1887.

Evans B. W., Johannes W., Oterdoom H. and Trommsdorff V. (1976) Stability of chrysotile and antigorite in the serpentinite multisystem. *Schweiz. Min. Pet. Mitt.* **56**, 79–93.

Evans B. W. and Trommsdorff V. (1972) Der Einfluss des Eisens auf die Hydratisierung von Duniten. *Schweiz. Min. Pet. Mitt.* **52**, 251–256.

Foustoukos D. I., Savov I. P. and Janecky D. R. (2008) Chemical and isotopic constraints on water/rock interactions at the Lost City hydrothermal field, 30°N Mid-Atlantic Ridge. *Geochim. Cosmochim. Acta* **72**, 5457–5474.

Frost B. R. (1985) On the stability of sulfides, oxides and native metals in serpentinite. *J. Petrol.* **26**, 31–63.

Frost B. R. and Beard J. S. (2007) On silica activity and serpentinization. *J. Petrol.* **48**, 1351–1368.

Früh-Green G. L., Kelley D. S., Bernasconi S. M., Karson J. A., Ludwig K. A., Butterfiled D. A., Boschi C. and Proskurowski G. (2003) 30,000 years of hydrothermal activity at the Lost City vent field. *Science* **301**, 495–498.

Früh-Green G. L., Connolly J. A. D., Plas A., Kelley D. S. and Grobety B. (2004) Serpentinization of oceanic peridotites: implications for geochemical cycles and biological activity. In *The Subsurface Biosphere at Mid-Ocean Ridges* (eds. W. S. D. Wilcock, E. F. DeLong, D. S. Kelley, J. A. Baross and S. C. Cary). Am. Geophys. Union, Washington, DC, pp. 119–136.

González-Mancera G., Ortega-Gutiérrez F., Nava N. and Arriola H. (2003) Mössbauer study of serpentine minerals in the ultramafic body of Tehuitzingo, southern Mexico. *Hyperf. Inter.* **148–149**, 61–71.

Helgeson H. C., Delany J. M., Nesbitt H. W. and Bird D. K. (1978) Summary and critique of the thermodynamic properties of rock-forming minerals. *Am. J. Sci.* **278A**, 1–229.

Holland T. J. B. (1989) Dependence of entropy on volume for silicate and oxide minerals: a review and a predictive model. *Am. Mineral.* **74**, 5–13.

Hostetler P. B., Coleman R. G., Mumpton F. A. and Evans B. W. (1966) Brucite in alpine serpentinites. *Am. Mineral.* **51**, 75–98.

Iyer K., Austrheim H., John T. and Jamtveit B. (2008) Serpentinization of the oceanic lithosphere and some geochemical consequences: constraints from the Leka Ophiolite Complex, Norway. *Chem. Geol.* **249**, 66–90.

Janecky D. R. and Seyfried, Jr., W. E. (1986) Hydrothermal serpentinization of peridotite within the oceanic crust: experimental investigations of mineralogy and major element chemistry. *Geochim. Cosmochim. Acta* **50**, 1357–1378.

Johnson J. W., Oelkers E. H. and Helgeson H. C. (1992) SUPCRT92: a software package for calculating the standard molal thermodynamic properties of minerals, gases, aqueous species, and reactions from 1–5000 bars and 0–1000 °C. *Comput. Geosci.* **18**, 899–947.

Jöns N., Bach W. and Schroeder T. (2009) Formation and alteration of plagiogranites in an ultramafic-hosted detachment fault at the Mid-Atlantic Ridge (ODP Leg 209). *Contrib. Mineral. Petrol.* **157**, 625–639.

Kaneda H., Takenouchi S. and Shoji T. (1986) Stability of pentlandite in the Fe–Ni–Co–S system. *Min. Depos.* **21**, 169–180.

Kelemen P., Kikawa E. and Miller D. J.Shipboard Scientific Party (2004a) ODP Leg 209 drills into mantle peridotite along the Mid-Atlantic Ridge from 14°N to 16°N. *JOIDES J.* **30**, 14–20.

Kelemen P. B., Kikawa E., Miller D. J., Abe N., Bach W., Carlson R. L., Casey J. F., Chambers L. M., Cheadle M., Cipriani A., Dick H. J. B., Faul U., Garces M., Garrido C., Gee J. S., Godard M. M., Graham D. W., Griffin D. W., Harvey J., Ildefonse B., Iturrino G. J., Josef J., Meurer W. P., Paulick H., Rosner M., Schroeder T., Seyler M. and Takazawa E. (2004b) Site 1274. In *Proceedings of the Ocean Drilling Program; Initial Reports; Drilling Mantle Peridotite along the Mid-Atlantic Ridge from 14° to 16°N; Covering Leg 209 of the Cruises of the Drilling Vessel JOIDES Resolution*; Rio de Janeiro, Brazil, to St. George, Bermuda; Sites 1268–1275, 6 May–6 July 2003. Texas A&M University Ocean Drilling Program, College Station, TX, United States. pp. 116.

Kelley D. S., Karson J. A., Blackman D. K., Früh-Green G. L., Butterfield D. A., Lilley M. D., Olson E. J., Schrenk M. O., Roe K. K., Lebon G. T. and Rivizzigno P.AT3-60 Shipboard Party (2001) An off-axis hydrothermal vent field near the Mid-Atlantic Ridge at 30°N. *Nature* **412**, 127–128.

Klein F. and Bach W. (2009) Fe–Ni–Co–O–S phase relations in peridotite seawater interactions. *J. Petrol.* **50**, 37–59.

Kretz R. (1983) Symbols for rock-forming minerals. *Am. Mineral.* **68**, 277–279.

McCollom T. M. (2000) Geochemical constraints on primary productivity in submarine hydrothermal vent plumes. *Deep-Sea Res. Lett.* **47**, 85–101.

McCollom T. M. and Bach W. (2009) Thermodynamic constraints on hydrogen generation during serpentinization of ultramafic rocks. *Geochim. Cosmochim. Acta* **73**, 856–875.

Moll M., Paulick H., Suhr G. and Bach W. (2007) Data report: microprobe analyses of primary phases (olivine, pyroxene, and spinel) and alteration products (serpentine, iowaite, talc, magnetite, and sulfides) in Holes 1268A, 1272A, and 1274A. In *Proceedings of the Ocean Drilling Program, Scientific Results*, 209 (eds. P. B. Kelemen, E. Kikawa and D. J. Miller). College Station, TX. pp. 1–13. doi: 10.2973/odp.proc.sr.209.003.2007.

Moody J. B. (1976) An experimental study on the serpentinization of iron-bearing olivines. *Am. Mineral.* **14**, 462–478.

Mottl M. J. (2002) Partitioning of energy and mass fluxes between mid-ocean ridge axes and flanks at high and low temperature. In *Dahlem Workshop on Energy and Mass Transfer in Marine Hydrothermal Systems* (eds. P. E. Halbach, V. Tunnicliffe and J. R. Hein). Freie Universitat Berlin, Berlin, Germany, pp. 271–286.

Nickel E. H. (1959) The occurrence of native nickel–iron in the serpentine rock of the Eastern Townships of Quebec Province. *Can. Mineral.* **6**, 307–319.

O'Hanley D. S. (1996) *Serpentinites: Records of Tectonic and Petrological History*. Oxford University Press, New York.

O'Hanley D. S. and Dyar M. D. (1993) The composition of lizardite 1T and the formation of magnetite in serpentinites. *Am. Mineral.* **78**, 391–404.

Olsen E. (1963) Equilibrium calculations in the system Mg, Fe, Si, O, H, and Ni. *Am. J. Sci.* **261**, 943–956.

Page N. J. (1967) Serpentinization at Burro Mountain, California. *Contrib. Mineral. Petrol.* **14**, 321–342.

Page N. J. (1968) Chemical differences among serpentine "polymorphs". *Am. Mineral.* **53**, 201–215.

Palandri J. L. and Reed M. H. (2004) Geochemical models of metasomatism in ultramafic systems: serpentinization, rodingitization, and sea floor carbonate chimney precipitation. *Geochim. Cosmochim. Acta* **68**, 1115–1133.

Paulick H., Bach W., Godard M., De Hoog J. C. M., Suhr G. and Harvey J. (2006) Geochemistry of abyssal peridotites (Mid-Atlantic Ridge, 15°20'N, ODP Leg 209): implications for fluid/rock interaction in slow spreading environments. *Chem. Geol.* **234**, 179–210.

Peretti A., Dubessy J., Mullis J., Frost B. R. and Trommsdorff V. (1992) Highly reducing conditions during Alpine metamorphism of the Malenco Peridotite (Sondrio, northern Italy) indicated by mineral paragenesis and H_2 in fluid inclusions. *Contrib. Mineral. Petrol.* **112**, 329–340.

Ransom B. and Helgeson H. C. (1994) Estimation of the standard molal heat capacities, entropies and volumes of 2:1 clay minerals. *Geochim. Cosmochim. Acta* **58**, 4537–4547.

Rozenson I., Bauminger E. R. and Heller-Kallai L. (1979) Mössbauer spectra of iron in 1:1 phyllosilicates. *Am. Mineral.* **64**, 893–901.

Sanford R. F. (1981) Mineralogical and chemical effects of hydration reactions and applications to serpentinization. *Am. Mineral.* **66**, 290–297.

Savov I. P., Ryan J. G., D'Antonio M. and Fryer P. (2007) Shallow slab fluid release across and along the Mariana arc-basin system: insights from geochemistry of serpentinized peridotites from the Mariana fore arc. *J. Geophys. Res.* **112**. doi:10.1029/2006JB004749.

Schmidt K., Koschinsky A., Garbe S. D., de Carvalho L. M. and Seifert R. (2007) Geochemistry of hydrothermal fluids from the ultramafic-hosted Logatchev hydrothermal field, 15°N on the Mid-Atlantic Ridge; temporal and spatial investigation. *Chem. Geol.* **242**, 1–21.

Seyfried, Jr., W. E., Foustoukos D. I. and Fu Q. (2007) Redox evolution and mass transfer during serpentinization; an experimental and theoretical study at 200 °C, 500 bar with implications for ultramafic-hosted hydrothermal systems at mid-ocean ridges. *Geochim. Cosmochim. Acta* **71**, 3872–3886.

Seyler M., Lorand J. P., Dick H. J. B. and Drouin M. (2007) Pervasive melt percolation reactions in ultra-depleted refractory harzburgites at the Mid-Atlantic Ridge 15°20'N; ODP Hole 1274A. *Contrib. Mineral. Petrol.* **153**, 303–319.

Shock E. L. and Helgeson H. C. (1988) Calculation of the thermodynamic and transport properties of aqueous species at high pressures and temperatures: correlation algorithms for ionic species and equation of state predictions to 5 kb and 1000 °C. *Geochim. Cosmochim. Acta* **52**, 2009–2036.

Shock E. L., Helgeson H. C. and Sverjensky D. A. (1989) Calculation of the thermodynamic and transport properties of aqueous species at high pressures and temperatures: standard partial molal properties of inorganic neutral species. *Geochim. Consmochim. Acta* **53**, 2157–2183.

Shock E. L., Sassani D. C., Willis M. and Sverjensky D. A. (1997) Inorganic species in geologic fluids: correlations among standard molal thermodynamic properties of aqueous ions and hydroxide complexes. *Geochim. Cosmochim. Acta* **61**, 907–950.

Sleep N. H., Meibom A., Fridiksson T., Coleman R. G. and Bird D. K. (2004) H_2-rich fluids from serpentinization: geochemical and biotic implications. *Proc. Natl. Acad. Sci. USA* **104**, 12818–12823.

Tagirov B. and Schott J. (2001) Aluminum speciation in crustal fluids revisited. *Geochim. Cosmochim. Acta* **65**, 3965–3992.

Trommsdorff V. and Evans B. W. (1972) Progressive metamorphism of antigorite schist in the Bergell tonalite aureole (Italy). *Am. J. Sci.* **272**, 423–437.

Wetzel L. R. and Shock E. L. (2000) Distinguishing ultramafic-from basalt-hosted submarine hydrothermal systems by comparing calculated vent fluid compositions. *J. Geophys. Res.* **105**, 8319–8340.

Whittaker E. J. and Wicks E. F. (1970) Chemical differences among the serpentine polymorphs: a discussion. *Am. Mineral.* **55**, 1025–1047.

Wicks F. J. and Plant A. G. (1979) Electron-microprobe and X-ray-microbeam studies of serpentine textures. *Can. Mineral.* **17**, 785–830.

Wilson J., Cressey G., Cressey B., Cuadros J., Ragnarsdottir K. V., Savage D. and Shibata M. (2006) The effect of iron on montmorillonite stability. (II) Experimental investigation. *Geochim. Cosmochim. Acta* **70**, 323–336.

Wolery T. J. (1992a) *EQ3/6, A Software Package for Geochemical Modeling of Aqueous Systems: Package Overview and Installation Guide (Version 7.0)*. Lawrence Livermore National Laboratory, Livermore, CA.

Wolery T. J. (1992b) *EQ3NR, A Computer Program for Geochemical Aqueous Speciation-Solubility Calculations: Theoretical Manual, User's Guide, and Related Documentation (Version 7.0)*. Lawrence Livermore National Laboratory, Livermore, CA.

Wolery T. J. and Daveler S. A. (1992) *EQ6, A Computer Program for Reaction Path Modelling of Aqueous Geochemical Systems: Theoretical Manual, User's Guide, and Related Documents*. Lawrence Livermore National Laboratory, Livermore, CA.

Wolery T. J. and Jarek R. L. (2003) *Software User's Manual EQ3/6 (Version 8.0)*. Sandia National Laboratories, Albuquerque, New Mexico.

Wolery T. J. and Jove-Colon C. F. (2004) *Qualification of Thermodynamic Data for Geochemical Modeling of Mineral–Water Interactions in Dilute Systems*. U.S. Department of Energy, Las Vegas, Nevada.

Associate editor: Jeffrey C. Alt